Research Square

Preprints are preliminary reports that have not undergone peer review.
They should not be considered conclusive, used to inform clinical practice,
or referenced by the media as validated information.

Coherent Intermode Energy Transfer and Wave–Particle Energy Partition in Reversed-Shear Alfvén Dynamics

Yu Yu

yu.yu@coios-ai.com

COIOS

Boqing Zhang

jacky.zhang@coios-ai.com

COIOS

Likai Tang

COIOS

Liqi Zhao

COIOS

Aiqun Wu

COIOS

Xiaolin Ge

COIOS

Jialun Huang

MACAO Doctoral Think Tank Association

Research Article

Keywords: Reversed-shear Alfvén eigenmodes, three-wave coupling, wave–particle energy exchange, energy partition, viscous dissipation

Posted Date: November 10th, 2026

DOI: https://doi.org/10.21203/rs.3.rs-11675019/v1

License: This work is licensed under a Creative Commons Attribution 4.0 International License.
Read Full License

Additional Declarations: The authors declare no competing interests.

Coherent Intermode Energy Transfer and Wave–Particle Energy Partition in Reversed-Shear Alfvén Dynamics

Yu Yu[1, 2, 3, #, *], Boqing Zhang[1, 2, 3, #, *], Likai Tang[1, 2, 3, #], Liqi Zhao[1, 2, 3], Aiqun Wu[1, 2, 3], Xiaolin Ge[1, 2, 3], Jialun Huang[4]

[1]COIOS (Hangzhou) Artificial Intelligence Co., Ltd., Hangzhou, China. [2]Hongkong Mac COIOS Technology, Co., Ltd., Hong Kong, China. [3]COIOS (Tianjin) Artificial Intelligence Co., Ltd., Tianjin, China. [4]Macao Doctoral Think Tank Association

Co-first author

* Correspondence: yu.yu@coios-ai.com; jacky.zhang@coios-ai.com

Abstract

Reversed-shear Alfvén eigenmodes (RSAEs) play an important role in energetic-particle transport and energy redistribution in magnetically confined fusion plasmas. Understanding their nonlinear evolution and potential suppression requires a consistent assessment of mode excitation, intermode energy transfer, wave–particle interactions, and dissipative processes. In this work, we investigate these mechanisms using a combination of global magnetohydrodynamic (MHD) responses and reduced theoretical and numerical models. We first examine phase-dependent energy transfer in a conservative three-wave interaction model, identifying the conditions governing energy exchange between symmetric pump-modes and a resonantly coupled daughter mode. We then investigate the temporal evolution of electromagnetic-field energy and species-resolved free-energy exchange in a local gyroaveraged electron–ion model. The results reveal alternating energy transfer between the thermal species and electromagnetic fields, with electron free-energy release, deuteron ion energy absorption, and polarization and magnetic-field energy storage contributing to the overall balance. An independent electrostatic electron-beam model further illustrates the relationship between electron free-energy release, electric-field growth, and subsequent partial reverse energy transfer. Additional calculations examine resonant particle-orbit interactions, phase-space trapping and distribution rearrangement, as well as the conversion of coherent wave energy into irreversible viscous dissipation. These results identify distinct mechanisms governing intermode energy transfer, particle–field exchange, phase mixing, and dissipative energy conversion. Taken together, the reduced models provide a framework for examining the individual components of RSAE-related energy redistribution and for identifying the quantities required for a self-consistent kinetic description. Establishing their combined influence on RSAE stability and suppression will require coupled simulations that simultaneously resolve wave-field evolution, resonant particle dynamics, species-resolved energy transfer, and radial particle transport. This leads to energy and transport diagnostics may provide useful physical constraints for future physics-informed inverse co-design framework of fusion-plasma operating conditions.

Introduction

In burning plasmas, the confinement of energetic particles is essential for effective energy deposition and sustained plasma heating. The transport and redistribution of these particles can be strongly influenced by Alfvénic instabilities. Alfvénic activity can alter the spatial distribution of that deposition and increase fast-ion transport [1]. RSAEs are Alfvén eigenmodes in reversed-shear equilibria, linking magnetic-shear control to fast-ion confinement and wave–particle energy exchange. Assessing instability suppression by reversed shear therefore requires determining how particle energy is transferred to the wave field, is redistributed among modes and is ultimately received by different species. Establishing the relationship between mode growth, damping, and the corresponding energy-transfer channels is essential for evaluating the effects of Alfvénic mode control on plasma heating and energetic-particle confinement.

Nonlinear interactions between Alfvén waves and resonant particles couple the evolution of wave fields and particle distributions: waves modify distribution gradients and particle orbits near resonance, and the rearranged distribution regulates the subsequent drive [2]. This phase-space framework provides a theoretical basis for analysing RSAE saturation. Frequencies and eigenfunctions specify the spatial and spectral structure, while phase-space evolution determines energy supply, return and transport. Integrating modal dynamics with phase-space evolution provides a framework for assessing how RSAE control influences fast-ion confinement and energy deposition into thermal species. This framework also motivates the joint optimization of equilibrium profiles and particle-source configurations.

Previous studies have identified several connected elements of RSAE control. Van Zeeland et al. found that electron cyclotron heating deposited near $q_{\min}$ suppresses RSAE activity in DIII-D, with stabilization, fast-ion profiles and neutron production depending on the deposition location [3]. Subsequent measurements and modelling showed improved fast-ion confinement for heating near the shear-reversal surface relative to on-axis heating, while relating spectra and radial mode structure to the equilibrium [4]. Using nonlinear gyrokinetic theory, Wei et al. derived RSAE excitation of zonal flows and currents and saturation through scattering into more stable radial eigenstates; their estimates for the burning-plasma parameters considered showed that zonal-current-induced continuum-frequency shifts can be comparable to the linear growth rate or frequency differences between radial eigenstates [5]. With energetic-particle dynamics retained as a linear response, Ma et al. found that beat-driven zonal current produces downward frequency chirping, enhances conversion into radially propagating kinetic Alfvén waves and electron Landau damping, and thereby provides a saturation channel [6]. Using a DIII-D equilibrium and profiles, global gyrokinetic simulations by Liu et al. showed that ion-temperature-gradient microturbulence scatters resonant fast ions and weakens RSAE-generated zonal flows. Relative to the RSAE-only calculation, cross-scale coupling reduces the initial saturation amplitude while increasing quasi-steady RSAE amplitude and fast-ion transport. The reciprocal RSAE effect reduces time-averaged thermal-ion heat transport through zonal flows and periodic changes in heat-flux direction [7]. These findings indicate mode suppression to energy conversion, particle reception and distribution evolution.

The central contribution of this study is to establish a mechanism-resolved framework for analyzing energy redistribution in reversed-shear Alfvénic systems. Rather than treating mode amplitude as a sufficient indicator of instability evolution, we investigate complementary mechanisms governing phase-dependent intermode energy transfer, species-resolved wave–particle energy exchange, resonant phase-space dynamics, and irreversible dissipation. Through a hierarchy of global and reduced numerical models, we identify the energy-transfer diagnostics and conservation constraints needed to connect these mechanisms within a future self-consistent kinetic description of RSAE dynamics.

The remainder of this paper is organized as follows. We first establish the reversed-shear equilibrium configuration and examine the corresponding global Alfvénic responses. We then investigate phase-controlled three-wave energy transfer and frequency-dependent coupling between daughter modes. Subsequently, we analyze species-resolved wave–particle energy exchange using local gyroaveraged and electrostatic kinetic models, followed by investigations of particle-orbit dynamics and resonant phase-space evolution. We finally examine continuum phase mixing and effective viscous dissipation, before discussing the implications of these complementary mechanisms for RSAE stability analysis and future physics-informed state estimation and inverse design.

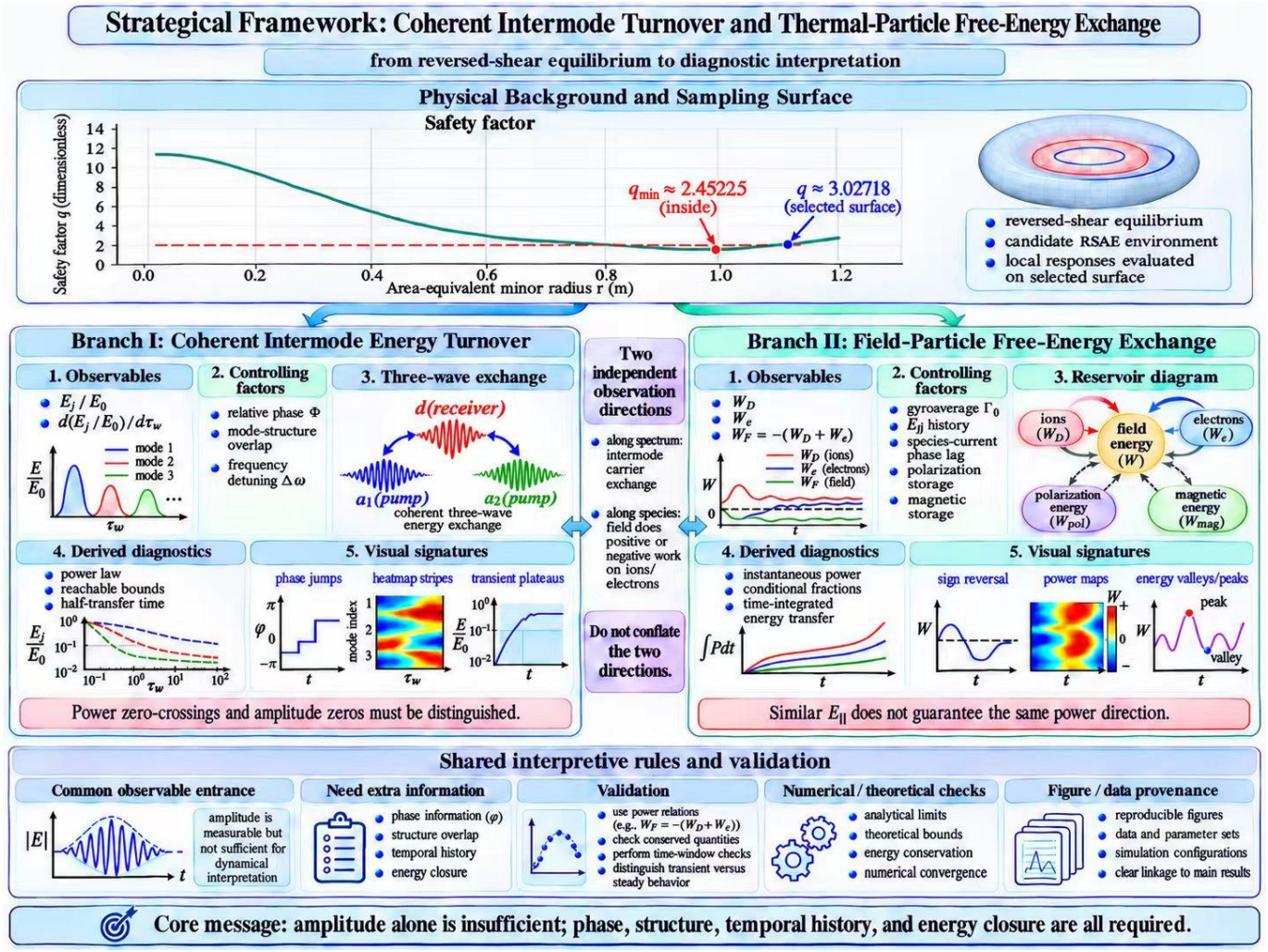


Figure 1 | Reversed-shear background, RSAE features and the two complementary energy-analysis pathways of this study. The upper panel shows the safety-factor profile of the reversed-shear equilibrium, identifying the internal minimum associated with the weak-shear localization region: $q_{\min} = 2.452$ provides the RSAE localization environment and the surface at $q = 3.027$ is used for the local thermal-species calculation. The two branches are phase-controlled three-wave intermode energy exchange and field–particle free-energy exchange, each listing its observables, controlling factors and visual signatures; the bottom row gives the interpretation and validation rules shared by both. Amplitude alone leaves the energy-transfer pathway undetermined; phase, structure, temporal history and energy closure must be examined together.

RSAE localization and probe placement

The safety factor $q(r)$ measures the ratio of toroidal to poloidal field-line turns. In a reversed-shear equilibrium, the safety-factor profile exhibits an internal minimum, across which the magnetic shear changes sign. The weak-shear region surrounding this minimum provides a favourable localization region for RSAEs. For toroidal number n and poloidal harmonic m, a local reference for the shear-Alfvén frequency is $\omega_A(r) \simeq v_A(r)|n - m/q(r)|/R$, where $v_A = B/\sqrt{\mu_0\rho}$. In the local approximation of slowly varying v_A/R, the minimum of q makes the first radial variation of the parallel wave number vanish, allowing neighbouring surfaces to maintain correlated oscillation phases over a broader region; toroidal coupling and particle responses then determine the radial structure and frequency [8]. RSAEs form around this weak-shear region, and changes in $q_{\min}$ produce frequency sweeping that provides spectroscopic information on the internal current profile [9,10]. The response of energetic particles with large orbits provides one mechanism for radial coupling [8]; finite-pressure and finite-Larmor-radius effects further modify the existence conditions and frequencies of the sweep-bottom and down-sweeping branches [11].

Figure 2 establishes the spatial sampling configuration of the probe: $q(r)$ decreases from the magnetic axis and rises beyond $q_{\min} = 2.452$, with the minimum surface in the outer part of the section. Centring the fast-particle probe envelope on that surface lets orbit sampling cover the weak-shear region and the main spatial extent of the candidate perturbation. The radial location of the excitation region is therefore selected with reference to the safety-factor minimum in the chosen equilibrium. The probe envelope is positioned to cover the corresponding weak-shear region as the equilibrium parameters vary. The thermal-species reception example uses a surface at $q = 3.027$ to resolve electron and deuteron ion responses through common-field powers.

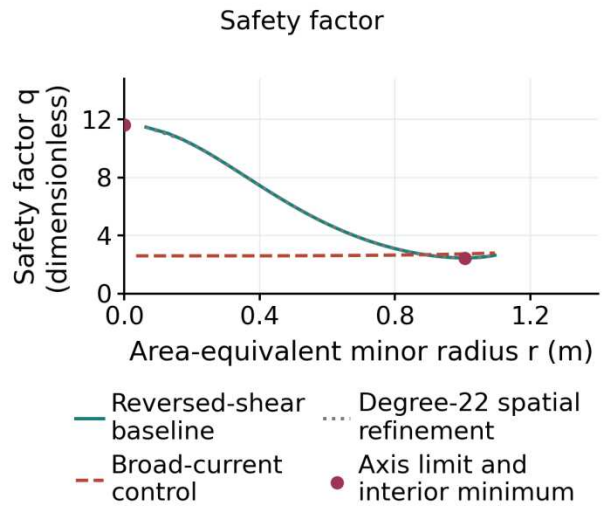


Figure 2 | Internal minimum of the safety-factor profile and reversal of magnetic shear. The horizontal axis is area-equivalent minor radius (m), and the vertical axis is the dimensionless safety factor q. The solid curve is the reversed-shear reference, and the dashed curve a broad-current comparison; circles mark the axis and internal minimum $q_{\min} = 2.452$. The solid curve changes from negative to positive slope across that minimum, corresponding to reversal of local magnetic shear. The local thermal-species common-field calculation samples another surface at $q = 3.027$; the parameters of that surface and of the minimum surface are reported separately. This panel supplies the equilibrium context for the RSAE spectral region.

The global ideal-MHD initial-value response adds dynamical information to this spatial sampling configuration. In Figure 3, a perturbation initialized near the q minimum produces an outer high-speed band, while the inner-radius initial-state control gives a different radial pattern, demonstrating the importance of overlap between the initial perturbation and the wave region. Colour measures root-mean-square velocity; its square weighted by density gives kinetic-energy weighting, with magnetic and compressional energy storage completing the modal energy. Near the minimum in the third panel, velocity starts at 2.627 m/s, falls at 40 μs to 0.861 m/s, and then at 80 μs reaches 1.363 m/s, reflecting multimode dephasing and return. The outer band retains the initial state's near-wall support, while radial basis changes produce corresponding changes in frequencies and spectral weights. These complementary global responses provide the spatial basis for selecting the radial extent and location of the particle probe.

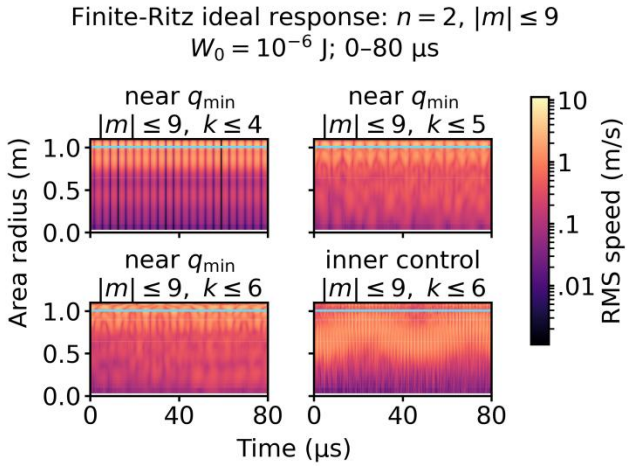


Figure 3 | global ideal-MHD initial-value response in a reversed-shear equilibrium. The horizontal axis is physical time t (μs, 0–80), and the vertical axis is area-equivalent minor radius r (m, approximately 0–1.10). All panels share a logarithmic colour scale for the vector RMS of the complex velocity amplitude, $|\mathbf{v}|_{\mathrm{rms}}$ (m/s), obtained by summing the squared magnitudes of its three components, averaging over the straight-field-line angle and taking the square root. The first three panels embed the same initial state near the q minimum in spaces with $|m| \le 9, k \le 4/5/6$; the lower-right panel uses an inner-radius state at $k \le 6$. Initial energy is 10^{-6} J in each case. The cyan line marks the sampled q minimum radius and the pale band a representative ideal-continuum crossing region.

The forced global displacement provides complementary phase information (Figure 4). On the $\varphi = 0$ section, positive and negative lobes of radial displacement ξ_R describe the spatial phase of one perturbation; the outer lobes constrain a candidate probe-field shape. Complex Fourier coefficients retain amplitude and phase together. The real part is the displacement projection at the chosen toroidal phase, and the imaginary part is its quadrature component, shifted by a quarter cycle. Both rotate with the phase origin and reconstruct the same real displacement through their conjugates; energy is determined by a quadratic form of the complete complex amplitude. An imposed body force controls the excitation location and frequency in this example.

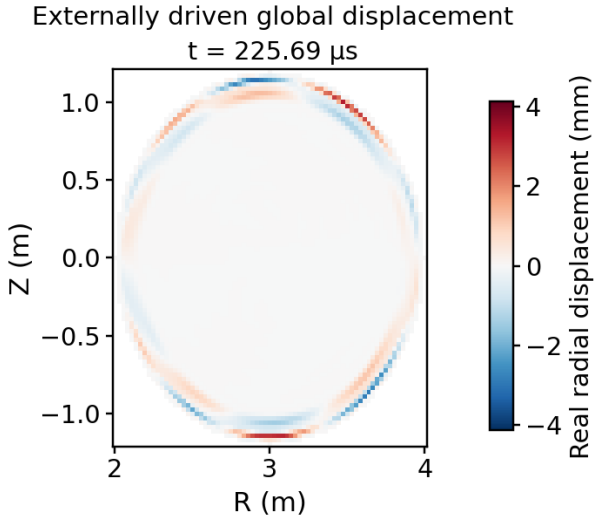


Figure 4 | Externally forced global displacement at $t = 225.7\,\mu s$. The horizontal axis is major radius R (m, approximately 2–4), and the vertical axis is Z (m, approximately -1.2–1.2). Colour gives the $\varphi = 0$ section real radial displacement ξ_R (mm): red positive, blue negative and white near zero. The time equals four source periods and the result starts from zero displacement. Alternating outer-region lobes and nodal lines show spatial displacement phase and can test shape overlap of a later probe in the outer radial region with a candidate field; the imaginary part is only a convention-dependent quadrature. This is a body-force response with source frequency 17.72 kHz and retained dominant frequency 16.30 kHz; the imposed body force specifies its energy input.

Results

The results follow an energy partition from electron-driven field excitation, where appropriate, through wave-partical energy exchange to background-ion energy absorption and dissipation, examining how it establishes a constraint for RSAE suppression. Global responses first establish spatial overlap between the probe in the outer radial region and the weak-shear region. The three-wave model then shows how relative phase controls the direction of pump–receiving-mode transfer, periodic return and high-energy states, while receiving-mode-frequency splitting opens an orthogonal energy storage channel. A local gyroaveraged model resolves powers among electrons, deuteron ions, polarization and magnetic energy storage, showing how ion energy absorption and electron free-energy release jointly determine changes in field energy. The electron-beam model exhibits strong early release, field growth and partial return; orbit and phase-space plots reveal resonance sampling, trapping and distribution rearrangement. Finally, continuum and viscous models place coherent energy redistribution and irreversible heat reception within their respective balances. Each figure group tests these elements under specified initial conditions and scales. Together they establish an energy-reception, dissipation and fast-ion-transport basis for assessing RSAE control and define the quantities required by phase-space kinetic simulations and physics-informed inverse co-design framework.

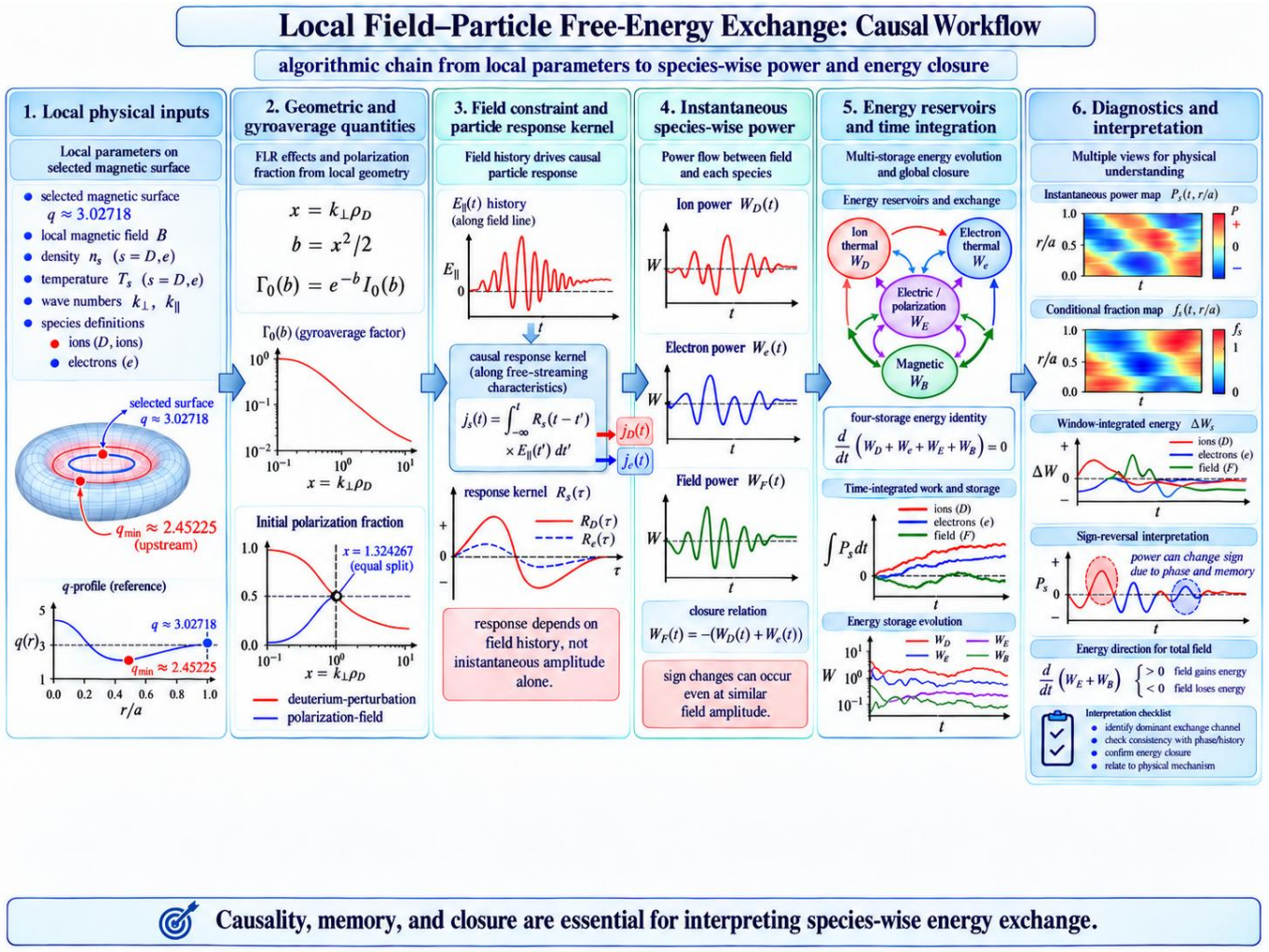


Figure 5 | The diagram illustrates the computational workflow for evaluating local field–particle energy exchange, from equilibrium and gyroaveraged inputs to causal species-current responses, instantaneous power calculations, energy integration, and closure diagnostics. The result emphasizes the roles of response memory, phase relationships, and energy conservation in determining species-resolved energy transfer.

Global response and probe placement

The shear reversal in Figure 2 can be related directly to wave propagation through a local expansion. Near $r_{\min}$, take $q(r) \simeq q_{\min} + 1/2\, q''_{\min}(r - r_{\min})^2$. Substitution into $k_\parallel = (n - m/q)/R$, treating R as constant over the narrow radial region, gives $k_\parallel \simeq (n - m/q_{\min})/R + m q''_{\min}(r - r_{\min})^2/(2R q^2_{\min})$. The first radial variation of the parallel wave number thus vanishes, and the second-order curvature sets the dephasing scale of neighbouring surfaces. Together with toroidal coupling and particle response, this weak-shear structure supports modes localized around the $q_{\min}$ surface [8,11]. The velocity bands in Figure 3 and displacement lobes in Figure 4 then test spatial overlap: a probe covering this finite-width region samples how different orbits encounter the same field shape.

The global ideal response first establishes the spatial structure of the perturbation and its conservative evolution. Expanding the displacement in a finite basis represents inertia and restoring forces by mass and restoring matrices, giving the following equation for the discrete displacement coefficients $\mathbf{c}$:

$$M\ddot{\mathbf{c}} + K_H \mathbf{c} = 0, \qquad K_H = 1/2\,(K_{\text{raw}} + K_{\text{raw}}^{\dagger}),$$
$$W = 1/4\left(\dot{\mathbf{c}}^{\dagger} M \dot{\mathbf{c}} + \mathbf{c}^{\dagger} K_H \mathbf{c}\right). \quad (1)$$

M is the mass matrix, K_{raw} the assembled restoring matrix and K_H its Hermitian part. The physical displacement is reconstructed as $\text{Re}(\boldsymbol{\xi} e^{in\varphi})$, giving the factor $1/4$ in the toroidally averaged quadratic energy. For fixed matrices in the ideal system, Hermitian restoring forces exchange kinetic and potential energy while preserving their sum. Figures 2–4 connect this evolution to the reversed-shear geometry: in Fig. 3, the velocity rms near the minimum starts at 2.627 m/s, falls at 40 μs to 0.861 m/s, and returns at 80 μs to 1.363 m/s. This decrease and recovery express multimode dephasing and recurrence, which change the local response over time.

The outer high-velocity band and displacement lobes show appreciable response in this region and, together with the geometry of $q_{\min}$, motivate testing orbital overlap there. Velocity colours describe local motion; full modal energy combines density-weighted kinetic energy with magnetic and compressional energy. Candidate frequencies and spectral weights vary substantially across the current nested bases, and the forced response retains a large source-projection error. We therefore use the spatial response of this finite discrete system to identify the region in which particle access and frequency selection are examined; Figs. 27–28 provide the corresponding orbital evidence. We next use an independent finite-mode model to study the direction of energy flow through a prescribed coupling channel.

Phase-controlled coherent exchange and recurrence

Quadratic terms in a weakly nonlinear perturbation multiply the fields of two waves, generating sum- and difference-frequency responses. When the sum frequency approaches the natural frequency of a third mode, spatial selection permits the interaction and the modal projection is nonzero, the interaction can accumulate over many carrier periods [12,13]. We therefore choose a reduced near-resonant three-wave model that retains slow exchange between two positive-energy modes a_1, a_2 with similar carrier frequencies and a receiving-mode d near twice that frequency, while rapidly oscillating terms contribute higher-order corrections. Figures 6–10 use this conservative normal form with a prescribed modal channel and coupling coefficient to examine how phase controls energy

flow. Together with the global response above, it supplies complementary descriptions of spatial structure and coherent exchange.

Here, a pump-mode denotes a wave mode that initially supplies energy to the nonlinear interaction. Its amplitude remains dynamical, so the model includes back-reaction from the receiving-mode. The two symmetric pump-modes have equal initial complex amplitudes and evolution equations of the same form under exchange of their indices. This symmetric initial condition ensures equal pump-mode action balances and allows the influence of the relative phase to be examined independently; the two labels represent two modal coordinates of the selected channel, and symmetry here refers to the initial state and the coupling equations. Each mode describes a collective field perturbation, while species-resolved energy balances are supplied by the particle models below. To retain both modal amplitude and phase, write the real perturbation as follows, where U_j is the mode structure, the complex envelope $C_j = X_j + iY_j$ evolves on the slow time T, and $\epsilon \ll 1$ measures the physical perturbation amplitude:

$$u = \epsilon \sum_{j=1}^{3} \left[C_j(T) U_j(\mathbf{x}) e^{-i\omega_j t} + C_j^*(T) U_j^*(\mathbf{x}) e^{i\omega_j t} \right] + O(\epsilon^2)$$

The conjugate term makes the field real. For a real component of the mode structure U_j, the modal contribution is $2\epsilon U_j[X_j \cos(\omega_j t) + Y_j \sin(\omega_j t)]$: the real and imaginary envelope components specify the cosine and sine quadratures of the same response, separated by a quarter period. Changing the carrier-phase origin rotates these coordinates, while modal intensity depends on the sum of their squares. The relative phase of the three envelopes determines the nonlinear work. Retaining the slowly accumulating product $C_1 C_2 C_3^*$ and its conjugate, normalizing the modes to positive action, and choosing phases that make the coupling real gives the following interaction Hamiltonian in a rotating frame:

$$H = \delta |d|^2 + 2g \,\mathrm{Re}(a_1 a_2 d^*), \quad i\dot{z}_j = \partial H / \partial z_j^*,$$
$$(z_1, z_2, z_3) = (a_1, a_2, d). \quad (2)$$

Here $g \geq 0$ is the dimensionless real coupling, $\delta = (\omega_3 - \omega_1 - \omega_2)/\kappa_0$ is the sum-frequency detuning, and overdots denote derivatives with respect to $\tau = \kappa_0 t$, where κ_0 is the reference nonlinear coupling rate. The detuning term describes phase drift of the receiving-mode relative to the pump-mode product, while the cubic interaction term produces bidirectional energy exchange. The slow-time approximation assumes carrier oscillations faster than envelope exchange and approximately fixed mode structures over the interval considered. Differentiating Eq. (2) with respect to each conjugate amplitude gives

$$\dot{a}_1 = -iga_2^* d, \quad \dot{a}_2 = -iga_1^* d, \dot{d} = -i\delta d - iga_1 a_2. \quad (3)$$

In Eq. (3), the pump-mode product drives the receiving-mode, while the product of the receiving-mode and the conjugate of the other pump-mode changes each pump-mode. Multiplying each equation by the corresponding conjugate amplitude and adding the conjugate of This leads to product gives the modal action rates: one unit of action lost by each pump-mode equals one unit gained by the receiving-mode. The system therefore has two Manley–Rowe invariants [12,13,14]:

$$N_1 = |a_1|^2 + |d|^2, \quad N_2 = |a_2|^2 + |d|^2, \quad \dot{N}_1 = \dot{N}_2 = 0. \quad (4)$$

Weighting by the carrier frequencies of the nearly equal-frequency pump-modes and the receiving-mode near twice that frequency gives $E_1 = |a_1|^2$, $E_2 = |a_2|^2$ and $E_d = 2|d|^2$, so that $E = E_1 + E_2 + E_d = N_1 + N_2$. This total is an exact invariant of the truncated system and a leading-order approximation to the near-resonant physical wave energy; finite-detuning and interaction corrections are described by the slow Hamiltonian H. Receiving-mode energy gain must therefore accompany pump-mode energy loss. Defining the three-wave phase as $\Phi = \arg(a_1 a_2 d^*)$ and substituting Eq. (3) into the energy derivatives gives the signed powers that determine the direction of energy flow:

$$P_d = 4g \,\mathrm{Im}(a_1 a_2 d^*) = 4g|a_1 a_2 d| \sin\Phi,$$
$$P_1 = P_2 = -P_d/2. \quad (5)$$

Define $P_j = \mathrm{d}E_j/\mathrm{d}\tau$. Equation (5) separates the transfer into an amplitude-dependent magnitude and a phase-dependent sign: for $0 < \Phi < \pi$, $P_d > 0$ and both pump-modes release energy; for $-\pi < \Phi < 0$, the receiving-mode returns energy to the pump-modes. The numerical solution reveals takes $g = 1$, $\delta = 0$ and $a_1(0) = a_2(0) = 1$; Fig. 6 uses four initial receiving-mode amplitudes $|d(0)| = 0.05, 0.15, 0.25, 0.5$ to evaluate P_d/E_0. Direct evaluation of the evolution equations follows the sinusoidal law, with the same zeros and extremal phases for all curves. Changing phase at fixed initial modal energies can therefore reverse the initial transfer direction; subsequent phase evolution can also make the initial pump-modes absorb energy again.

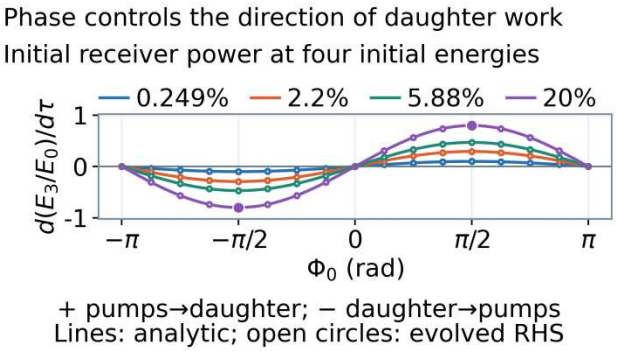


Figure 6 | Dependence of instantaneous three-wave energy transfer on relative phase. The horizontal axis is the initial phase Φ_0 and the vertical axis is $\mathrm{d}(E_d/E_0)/\mathrm{d}\tau$, where $\tau = \kappa_0 t$ and E_0 is the initial total carrier energy of each case. Positive values indicate transfer from a_1, a_2 to d; negative values indicate the reverse. The legend gives the initial receiving-mode-energy fraction for each curve. Solid curves show Eq. (5), and open symbols directly evaluate the evolution-equation right-hand side. Power crosses zero at $\Phi_0 = 0, \pm\pi$ and has opposite extreme at $\Phi_0 = \pm\pi/2$. Curve heights depend on both initial amplitudes and the total-energy normalization. The figure uses $d_3 = d$ and $E_3 = E_d$.

The instantaneous power also determines how receiving-mode energy approaches a high value. At exact resonance with symmetric pump-modes, a particular initial-phase choice permits a real-valued representation $a_1 = a_2 = A$ and $d = -ib$. Equation (3) becomes $\dot{A} = -gAb$, $\dot{b} = gA^2$, while preserving $I = A^2 + b^2 = 1 + b_0^2$. The initial state $A(0) = 1$, $b(0) = b_0 > 0$ corresponds to $\Phi_0 = +\pi/2$: the pump-modes gradually release energy and the the daughter-mode energy increases monotonically. Eliminating the pump-mode amplitude with the action invariant gives the directly integrable trajectory tested in Fig. 7:

$$b = \sqrt{I}\tanh u, \quad A = \sqrt{I}\,\mathrm{sech}\,u, u = g\sqrt{I}\tau + \mathrm{atanh}(b_0/\sqrt{I}). \quad (6)$$

Equation (6) also holds for $b_0 < 0$, corresponding to $\Phi_0 = -\pi/2$. Figure 7 compares numerical complex-amplitude evolution with these two analytic branches. For positive initial phase, receiving-mode energy increases immediately and then approaches a plateau as the pump-modes deplete. For negative initial phase, the receiving-mode first returns stored energy to the pump-modes and then gains energy, reaching the same half-pump-mode transfer condition about 73% later. Complex amplitude, energy and power remain continuous when the receiving-mode amplitude crosses zero, while the argument coordinate becomes singular. Both extended high-energy intervals arise from conservative separatrix approach to pump-mode depletion: the interaction power tends to zero as the pump-mode amplitudes decrease.

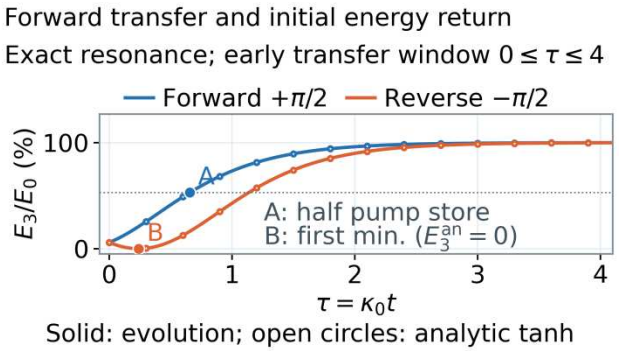


Figure 7 | Dependence of daughter-mode energy evolution on the initial three-wave phase. The horizontal axis is $\tau = \kappa_0 t$ and the vertical axis is E_d/E_0 in percent. The blue curve shows sustained pump-to-receiving-mode transfer. The orange curve first returns the initial stored receiving-mode energy to the pump-modes and then gains energy. Solid curves show numerical complex-amplitude evolution; open symbols show the analytic solution of Eq. (6). Point A at $\tau = 0.6560$ marks a net receiving-mode gain equal to half the initial total pump-mode energy. Point B at $\tau = 0.2401$ is the first minimum for the reverse initial phase. The figure uses $E_3 = E_d$.

For general initial phases, the interaction power changes sign during evolution. Figures 7–10 use $|d(0)| = 0.25$. Scanning the initial phase at fixed initial modal energies and integrating over $0 \le \tau \le 12$ gives the repeated high- and low-energy bands in Fig. 8. Rising receiving-mode energy indicates release from the pump-modes to d; falling receiving-mode energy indicates return from d to the pump-modes. Trajectories close to $\Phi_0 = \pm\pi/2$ spend long intervals at high energy, connecting to the asymptotic separatrix behaviour in Fig. 7. To explain this phase-dependent return time, we next use the invariants to determine the accessible receiving-mode-energy interval.

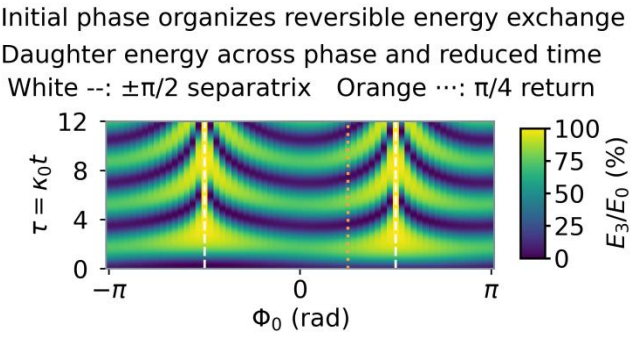


Figure 8 | Initial-phase dependence of recurrent energy exchange. The horizontal axis is Φ_0 and the vertical axis is $\tau = \kappa_0 t$; the common colour scale gives E_d/E_0 in percent. Alternating bright and dark bands along time indicate increases and decreases in receiving-mode energy storage. White dashed lines mark the separatrix phases $\Phi_0 = \pm\pi/2$; neighbouring extended high-energy bands correspond to slow evolution near pump-mode depletion. The orange dotted line illustrates repeated exchange on a general trajectory. The colour scale uses $E_3 = E_d$.

For symmetric initial states, the two action invariants are equal, $N_1 = N_2 = I$. Writing the receiving-mode intensity as $n = |d|^2$ gives intensity $I - n$ for each pump-mode: every unit of receiving-mode action gain reduces the pump-mode intensity available for subsequent exchange. At exact resonance, the Hamiltonian also gives the constant $h = \mathrm{Re}(a_1 a_2 d^*) = b_0 \cos\Phi_0$. Combining this constraint with $\dot{n} = 2g\,\mathrm{Im}(a_1 a_2 d^*)$ reduces the complex-amplitude evolution to

$$\dot{n}^2 = 4g^2[n(I-n)^2 - h^2],$$

$$n(I-n)^2 = h^2 \quad (\dot{n} = 0). \quad (7)$$

Equation (7) maps the initial phase, through h, into an accessible receiving-mode-energy interval. Action conservation and nonnegative pump-mode intensities require $0 \le n \le I$ and $|a_1|^2 = |a_2|^2 = I - n$. Within this physical interval, accessible roots of $n(I-n)^2 = h^2$ give zero-power boundaries. A general trajectory lies between the lower and upper simple roots and satisfies $n(I-n)^2 - h^2 \ge 0$. The upper bound is therefore constrained by both initial energy and three-wave phase, while the initial power sign selects which boundary the trajectory approaches first.

Figure 9 replots the same trajectories as Fig. 8 in the energy–power plane, making physical interpretation of turning points explicit. In the upper half-plane, $P_d > 0$: both pump-modes release energy and receiving-mode energy storage grows. After the high-energy turning point, the trajectory enters the lower half-plane with $P_d < 0$: the receiving-mode releases energy and the pump-modes absorb it again. Closed loops between two simple roots represent finite-period exchange. The purple separatrix with $\Phi_0 = +\pi/2$ instead approaches $E_d/E_0 = 100\%$ asymptotically. Pump-mode amplitudes and exchange power tend to zero together at the endpoint, and the time required to reach it diverges. A high receiving-mode-mode energy accompanied by a small instantaneous transfer power identifies a slowly evolving segment of the conservative exchange trajectory.

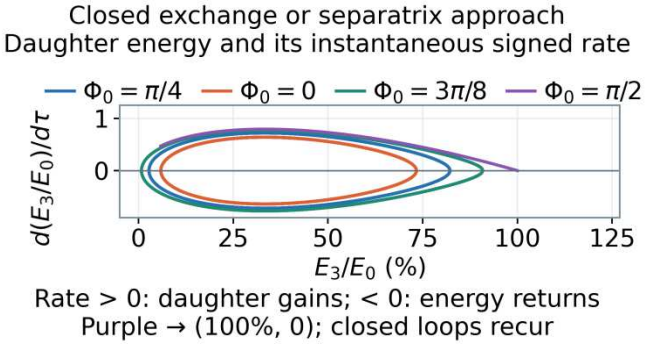


Figure 9 | Energy-power trajectories illustrating periodic exchange and separatrix dynamics. The horizontal axis is E_d/E_0 in percent and the vertical axis is $\mathrm{d}(E_d/E_0)/\mathrm{d}\tau$, where $\tau = \kappa_0 t$; the ordinate uses the rate of change of the energy fraction. The upper half-plane corresponds to pump-to-receiving-mode transfer, and the lower half-plane to return from the receiving-mode. Intersections with the zero-power axis are determined by the accessible roots of Eq. (7) within $0 \le n \le I$. Closed loops represent finite-period exchange between simple roots; the purple separatrix asymptotically approaches the zero-power endpoint at $E_d/E_0 = 100\%$. The figure uses $E_3 = E_d$.

Figure 10 compares the turning bounds from Eq. (7) with extrema actually visited during the finite observation window. Every trajectory starts with a receiving-mode fraction of 5.88%, yet initial phase changes the accessible upper bound: 73.35% at zero phase, 82.20% at a quarter-pi phase, and, for $\Phi_0 = +\pi/2$, an asymptotic 100%. Simple roots give finite-time turning points, whereas a repeated root gives an infinite-time asymptotic endpoint. This comparison shows that phase changes both transferable energy and its arrival time through the invariants. These conservative trajectories themselves produce extended high-energy intervals over a finite window.

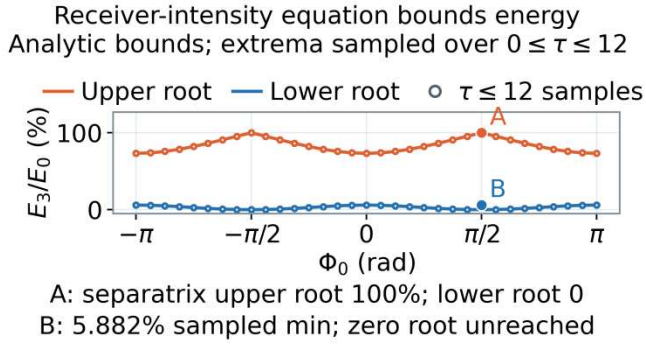


Figure 10 | Initial phase bounds accessible receiving-mode energy and finite-window extreme. The horizontal axis is Φ_0 and the vertical axis is E_d/E_0 in percent. Upper and lower solid curves give physical boundaries from Eq. (7) within $0 \le n \le I$; open symbols are extrema sampled over $0 \le \tau \le 12$. As $\Phi_0 \to \pm\pi/2$, $h \to 0$ and the upper bound approaches 100%. The forward-separatrix window minimum equals the initial receiving-mode fraction while the analytic lower bound tends to zero, showing how the initial direction of motion

constrains the range visited during the window. The figure uses $d_3 = d$ and $E_3 = E_d$.

These results establish a causal chain for coherent exchange: the three-wave phase fixes the power sign, action conservation constrains energy fractions, and the Hamiltonian further determines turning points. For $h = 0$, the repeated root at $n = I$ in Eq. (7) gives the separatrix of Eq. (6). For $h \neq 0$ with separated accessible roots, power reverses at the turning points and produces recurrent exchange. The time bands in Fig. 8, energy–power trajectories in Fig. 9 and turning bounds in Fig. 10 show complementary views of this structure. This conservative baseline provides a comparison for the later inclusion of particle reception and dissipation: each additional channel is quantified through its received energy together with the total balance.[1]

Orthogonal receiving-mode decomposition and frequency splitting

The same pump-mode pair can couple to multiple receiving-modes, in which case the coupling coefficients determine the directly driven direction of energy flow. Let two receiving-modes d_3, d_4 share the pump-mode pair, with the same positive-action normalization and real couplings g_3, g_4. The combination B along the coupling vector directly receives the pump-mode drive; the orthogonal combination D describes another receiving-mode degree of freedom. Projecting the receiving-mode equations onto these directions, for equal couplings and symmetric detunings $+\Delta/2$ and $-\Delta/2$ about the mean resonance frequency, gives

$$B = \frac{g_3 d_3 + g_4 d_4}{K},$$

$$D = \frac{g_4 d_3 - g_3 d_4}{K},$$

$$K = \sqrt{g_3^2 + g_4^2}, \dot{B} = -iKa_1 a_2 - i\frac{\Delta}{2}D,$$

$$\dot{D} = -i\frac{\Delta}{2}B \quad (g_3 = g_4). \quad (8)$$

Here $K > 0$ and $\Delta = \Delta_\omega/\kappa_0$. At exact degeneracy with zero common detuning, the pump-modes directly drive B while D keeps its initial value. If both receiving-modes are initially empty, then whenever their total energy is nonzero, $E_3/(E_3 + E_4) = g_3^2/(g_3^2 + g_4^2)$: the two receiving-mode amplitudes share the energy of one driven combination according to their coupling weights. This degenerate limit supplies the baseline for the frequency-splitting calculation and shows why identifying reception channels involves both modal coordinates and drive directions.

Finite frequency splitting interconverts B, D through the off-diagonal terms of Eq. (8), allowing energy that enters the driven combination to move into the orthogonal combination. Figure 11 uses equal couplings and identical initial receiving-mode seeds, so that D is initially zero, and scans $\Delta = \Delta_\omega/\kappa_0$. Orthogonal energy remains zero at zero splitting; finite splitting produces alternating bands of energy storage and return. Their dependence on accumulated relative phase $\Delta_\omega t$ reflects competition between the frequency separation and the pump-exchange time. These results demonstrate that frequency splitting can redistribute energy between the directly driven and orthogonal receiving-mode combinations, leading to time-dependent energy storage in the orthogonal modal component.

[1] The numerical implementations, discretization schemes, initial and boundary conditions, parameter choices, and numerical-convergence assessments are described in the Methods section. The governing equations and definitions of the relevant physical quantities are provided in the main text.

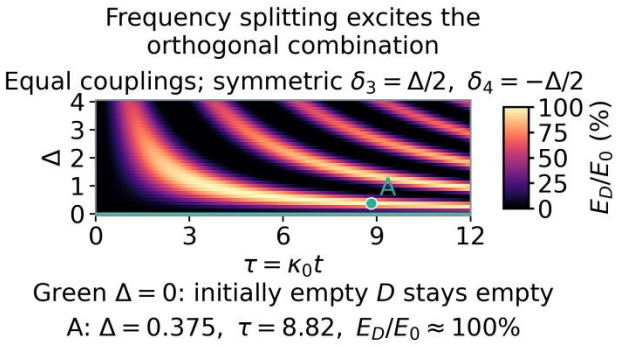


Figure 11 | Frequency splitting induces energy transfer into the initially unexcited orthogonal mode. The two receiving-modes have equal couplings, detunings $+\Delta/2$ and $-\Delta/2$ about the mean resonance frequency, and identical initial seeds. The horizontal axis is $\tau = \kappa_0 t$ and the vertical axis is $\Delta = \Delta_\omega/\kappa_0$. Colour gives orthogonal-combination energy E_D/E_0 in percent, where E_0 is the initial total carrier energy of the four modes. The zero-splitting baseline keeps $D = 0$; finite splitting produces coherent exchange between B, D. Point A at $\Delta = 0.375$, $\tau = 8.82$ is the sampled maximum on this grid and time window, displayed as 100% at the plotted precision. Colour represents transient energy storage in the conservative four-mode system.

For the physical interpretation of RSAE spectra with multiple peaks, these results motivate comparing coupling directions, relative phases and frequency separations together. In the model, spectral-weight migration arises from coherent energy flow between driven and orthogonal combinations, so receiving-mode amplitudes contain contributions from both direct drive and internal redistribution. Applying this mechanism to a specific RSAE assigns the physical identity of each combination through global mode structures and coupling projections; particle work, damping and outward energy flux determine the eventual energy-transfer pathway. The following analysis therefore turns to particle–field exchange to quantify reception beyond modal energy storage.

thermal-species response to a self-consistent electromagnetic field

Three-wave trajectories describe exchange by mode; identifying particle reception requires partitioning electromagnetic exchange into field and species contributions. Figures 12–20 isolate this partition in a local thermal-electron–ion model, with both species determining the scalar and vector potentials. The result starts from an ion-distribution perturbation, establishes initial polarization energy storage through the field constraint, and evolves free-energy exchange among electrons, deuteron ions and their common field. This sequence addresses why species responses differ in time, how electron free-energy release is divided between ions and field, and how instantaneous powers accumulate into stored energies. Early electron energy supply is examined later with an independent electron-beam model.

The common-field response combines particle free streaming with acceleration by the parallel electric field. Let F_{0a} be a zero-flow Maxwellian background, g_a its linear perturbation and $h_a = g_a/F_{0a}$. The local, uniform, collisionless low-frequency reduction retains parallel free streaming and gyroaveraged electric acceleration [15,16,17]:

$$(\partial_t + \mathrm{i}k_\parallel v_\parallel) g_a = \frac{q_a F_{0a}}{T_a} G_a v_\parallel E_\parallel. \quad (9)$$

$$E_\parallel = -\mathrm{i}k_\parallel \phi - \partial_t A_\parallel. \quad (10)$$

Here q_a, m_a and T_a denote the species charge and mass, and the temperature expressed in joules, respectively. The ion gyrofrequency is $\Omega_D = eB/m_D$ and its gyroaverage is $G_D = J_0(k_\perp v_\perp/|\Omega_D|)$; electrons have $G_e = 1$ at the scales considered. Charge and current deposition use the same gyroaverage. Quasineutral polarization and parallel Ampère constraints, with displacement current neglected, give

$$C_\Sigma \phi = \sum_a q_a \int G_a g_a \, \mathrm{d}^3 v,$$

$$\frac{k_\perp^2}{\mu_0} A_\parallel = \sum_a q_a \int v_\parallel G_a g_a \, \mathrm{d}^3 v. \quad (11)$$

The polarization coefficient is $C_\Sigma = \sum_a (q_a^2 n_a / T_a)(1 - \langle G_a^2 \rangle_a)$, where brackets denote normalized velocity averages over each species Maxwellian. With $G_e = 1$, deuteron ions provide the polarization in this model. The potentials are determined together by the particle response; both electrostatic and inductive contributions to the electric field enter the species power.

Complex fields use the real-part reconstruction convention, with the physical harmonic $\mathrm{Re}(\hat{u} e^{i k_\parallel z})$. Averaging a quadratic quantity over a complete spatial period supplies a factor $1/2$; together with the quadratic-energy coefficient, the perturbation free energy in the reference volume $V = 1\,\mathrm{m}^3$ is

$$W = \frac{V}{4}\left[\sum_a n_a T_a \langle |h_a|^2 \rangle_a + C_\Sigma |\phi|^2 + \frac{k_\perp^2}{\mu_0} |A_\parallel|^2\right] \equiv W_D + W_e + W_{\mathrm{pol}} + W_{\mathrm{mag}}. \quad (12)$$

W_D and W_e measure the quadratic free energy of distribution perturbations relative to the Maxwellian backgrounds; W_{pol} is polarization energy storage and W_{mag} is magnetic energy storage associated with the total parallel current. The species parallel current is $j_a = q_a \int v_\parallel G_a g_a \, \mathrm{d}^3 v$. Multiplying Eq. (9) by $T_a h_a^*$, integrating in velocity space, taking the real part and applying the two constraints in Eq. (11) gives

$$P_a = \frac{V}{2} \mathrm{Re}(E_\parallel j_a^*),$$
$$P_F = \dot{W}_{\mathrm{pol}} + \dot{W}_{\mathrm{mag}} = -(P_D + P_e),$$
$$\dot{W} = 0. \quad (13)$$

Here $P_a > 0$ denotes free-energy transfer from the field to species a, and $P_a < 0$ denotes release by that species. combined electromagnetic-field energy is $W_F = W_{\mathrm{pol}} + W_{\mathrm{mag}}$. The species terms are quadratic distribution free energies and the field terms are polarization and magnetic energy storage; these are distinct from heat. Writing $E_\parallel = |E| e^{\mathrm{i}\theta_E}$ and $j_a = |j_a| e^{\mathrm{i}\theta_a}$ gives $P_a = (V/2)|E||j_a| \cos(\theta_E - \theta_a)$. The complex representation retains the field–current phase difference, and the real part selects the in-phase component that does work under the real-harmonic average.

Free streaming gives particles with different parallel velocities different accumulated phases, so the later current produced by an electric-field impulse depends on species thermal speed. This memory follows directly from Eq. (9): integration along parallel free-streaming characteristics gives the contribution of field history to the distribution perturbation at the observation time:

$$g_a(v,t) = e^{-\mathrm{i} k_\parallel v_\parallel t} g_a(v,0) + \frac{q_a F_{0a}}{T_a} G_a v_\parallel \int_0^t e^{-\mathrm{i} k_\parallel v_\parallel (t-s)} E_\parallel(s) \, \mathrm{d}s. \quad (14)$$

The first term produces the ballistic current j_a^{h} set by the initial distribution; combining it with the field-driven contribution gives $j_a(t) = j_a^{\mathrm{h}}(t) + \int_0^t K_a(t-s) E_\parallel(s) \, \mathrm{d}s$. The causal kernel after Maxwellian velocity averaging is

$$K_a(u) = \frac{n_a q_a^2 \Gamma_a}{m_a}\left[1 - \frac{(k_\parallel v_{\mathrm{th},a} u)^2}{2}\right] e^{-(k_\parallel v_{\mathrm{th},a} u)^2/4},$$
$$\Gamma_D = \Gamma_0(x),$$
$$\Gamma_e = 1. \quad (15)$$

Here $u = t - s \geq 0$ is the response lag. Figure 12 compares analytic kernels with velocity quadrature using $\Delta\tau = k_\parallel v_{\mathrm{th},e} u$: the electron kernel crosses zero at $\sqrt{2}$ and reaches −44.63% at $\sqrt{6}$, whereas the deuteron ion kernel retains 70.13% at $\Delta\tau = 40$. The different thermal velocities of electrons and deuteron ions produce distinct temporal response kernels, resulting in species-dependent current phases under the same electromagnetic-field history. The negative lobe indicates that the current response to an earlier electric-field impulse becomes out of phase with the applied field at the corresponding time lag. Actual power direction follows from the complete field history, ballistic current and present field through Eq. (13).

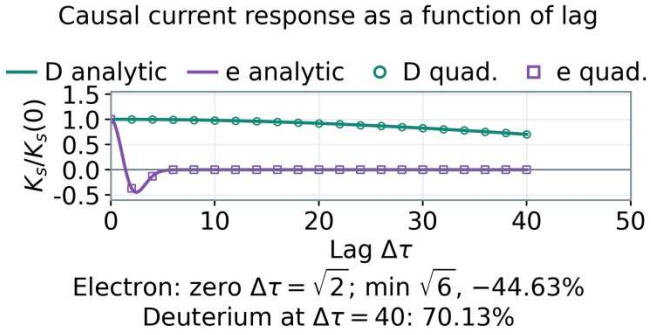


Figure 12 | Causal current kernels of thermal electrons and deuterium ions. The abscissa is lag $\Delta\tau = k_\parallel v_{\mathrm{th},e} u$, with $u = t - s \geq 0$; the ordinate $K_a(u)/K_a(0)$ is normalized to each species' zero-lag value. Solid lines give the zero-flow Maxwellian analytic kernels of Eq. (15), and symbols give velocity quadrature. Zero crossings separate in-phase and out-of-phase impulse contributions to current.

Gyroaveraging also sets the energy partition of a specified initial state. The thermal gyroradius is $\rho_D = \sqrt{2T_D/m_D}/|\Omega_D|$. For $x = k_\perp \rho_D$, $y = m_D v_\perp^2/(2T_D)$ and $b = x^2/2$, the first and second Maxwellian gyroaverages are

$$M_1(x) = \int_0^\infty e^{-y} J_0(x\sqrt{y}) \, \mathrm{d}y = e^{-x^2/4},$$
$$\Gamma_0(x) = \int_0^\infty e^{-y} J_0^2(x\sqrt{y}) \, \mathrm{d}y = e^{-b} I_0(b). \quad (16)$$

Thus $C_D = (e^2 n_D/T_D)[1 - \Gamma_0(x)]$. The long-wavelength expansion $\Gamma_0 = 1 - x^2/2 + 3x^4/16 + O(x^6)$ gives the usual finite-Larmor-radius asymptote. Since x extends to 1.5 here, the calculation uses the full I_0 expression in equation (16). A more direct testable prediction follows from our initial state: taking $h_D(0) = \epsilon G_D$, $h_e(0) = 0$ and $A_\parallel(0) = 0$, equation (11) gives $e\phi(0)/T_D = \epsilon\Gamma_0/(1 - \Gamma_0)$. Substitution into the quadratic ion and polarization energies gives

$$\frac{W_{\mathrm{pol}}(0)}{W(0)} = \Gamma_0(x),$$
$$\frac{W_D(0)}{W(0)} = 1 - \Gamma_0(x),$$
$$W(0) = \frac{V n_D T_D \epsilon^2}{4} \frac{\Gamma_0(x)}{1 - \Gamma_0(x)}. \quad (17)$$

Figure 13 compares this initial-state relation with 11 solved points. Shortening the perpendicular field scale increases x and decreases Γ_0, shifting energy storage from polarization to the deuteron ion distribution; the shares are equal at $x = 1.324$. Analytic continuation over the extended range gives polarization-field and ion-perturbation shares of 5.66% and 94.34% at $x = 10$. These fractions use $h_D(0) = \epsilon G_D$ as the initial condition. At small x, the ion share vanishes as $x^2/2$ and the polarization share approaches unity. The fixed-perturbation field constraint is singular at $x = 0$, so the subsequent common-field evolution uses $0.5 \leq x \leq 1.5$. Gyro-averaging thus sets both the initial partition and the perpendicular scale of species coupling.

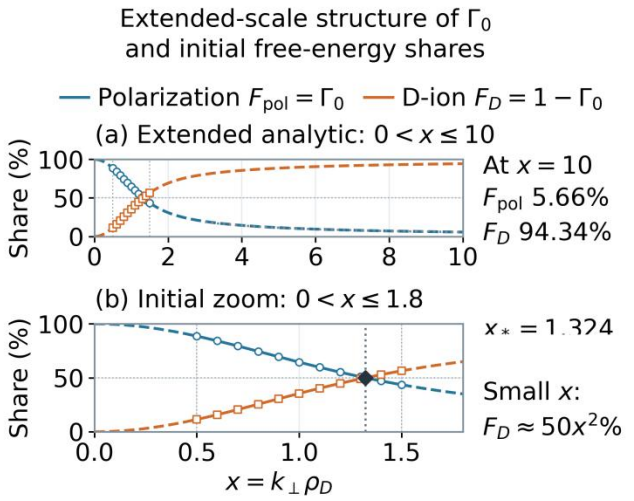


Figure 13 | Gyro-averaging dependence of the initial free-energy partition. The abscissa is $x = k_\perp \rho_D$; upper and lower panels span $0 < x \leq 10$ and $0 < x \leq 1.8$, with initial free-energy share (%) on the ordinate. Blue denotes $F_{pol} = \Gamma_0(x)$ and orange $F_D = 1 - \Gamma_0(x)$, where $\Gamma_0(x) = e^{-x^2/2} I_0(x^2/2)$. Over $0.5 \leq x \leq 1.5$, solid curves and open symbols give the analytic expression and solved points; dashed extensions continue the analytic expression. The black diamond marks equal shares, and the grey dotted curve gives the large-x asymptote $100/(\sqrt{\pi}x)$.

Partition of electron free-energy release and electromagnetic-field energy storage

With the initial partition and causal response kernels established, Eq. (13) converts species-phase evolution into transfer directions. The common-field calculation produces the alternating power bands in Figure 14: the in-phase projection of ion current onto the field determines P_D, and the summed species-current projections determine $P_F = -(P_D + P_e)$. At $x = 1$, the main intervals of field gain are approximately 2.9–5.6, 8.4–11.1, 13.8–16.5 and 19.4–21.7 μs; the electromagnetic field supplies the remaining energy required for ion absorption in adjacent intervals. When electron free-energy release exceeds simultaneous ion energy absorption, the remainder accumulates in the field; when ion energy absorption exceeds electron free-energy release, electromagnetic-field energy storage supplies the deficit. The instantaneous energy-balance relation provides the physical interpretation of the alternating regions of field-energy gain and loss.

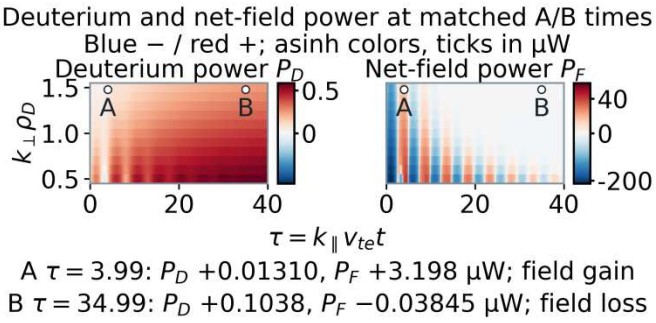


Figure 14 | Instantaneous powers of deuterium ions and the combined field. The axes are $\tau = k_\parallel v_{th,e} t$ and $x = k_\perp \rho_D$, scanned over 0.5–1.5. Left and right colours give P_D and $P_F = -(P_D + P_e)$ in microwatts for reference volume $1\ m^3$. Red is positive, blue negative and white near zero; colour scales use inverse-hyperbolic-sine compression. Positive values indicate ion and combined electromagnetic-field gain, respectively. A and B lie at $x = 1.5, \tau = 3.99$ and 34.99, matching the states in Figures 15–16.

The main case at $x = 1$ supplies three quantities with different denominators (Table 1). Among electron-to-field transfer midpoints, **30.54%** also satisfy $P_F > 0$; at the remaining **69.46%**, ion absorption exceeds electron free-energy release. This is a conditional time fraction. Separate integrals of positive and negative field power over the full window give gross particle-to-field transfer equal to **21.27%** of gross field-to-particle transfer; their difference gives net transfer from the field to thermal species. Selecting all $P_F > 0$ midpoints instead partitions electron free-energy release into **96.21%** entering the combined field and **3.789%** entering the deuterium perturbation. Field gain is predominantly polarization energy, with a smaller net magnetic change. This is energy partition within a selected midpoint set. Figures 15–16, 20 show these conditions, transfer directions and integrated powers.

Table 1 | Definitions of field–particle transfer diagnostics at x = 1.

Diagnostic	Definition	Result
Electron release	763 / 1000 midpoints	76.30%
Field gain during electron release	233 / 763 midpoints	30.54%
Field loss during electron release	530 / 763 midpoints	69.46%
Field → particles (gross)	$G_{out} = \Sigma[-P_F]_+ \Delta t$	135.6 pJ
Particles → field (gross)	$G_{in} = \Sigma[P_F]_+ \Delta t$	28.84 pJ
Return relative to outward transfer	G_{in} / G_{out}	21.27%
Field share during field gain	G_{in} / E_{rel}	96.21%
Deuteron share during field gain	$(\Sigma_S P_D \Delta t) / E_{rel}$	3.789%
Net field-to-particle transfer	$G_{out} - G_{in}$	+106.7 pJ
Change in field energy	$W_F(T) - W_F(0)$	−106.7 pJ

Powers are sampled at the midpoints of 1000 equal steps over 0–44.53 μs. Electron release has $P_e < 0$. Field gain has $P_F = -(P_D + P_e) > 0$. The set S contains the 233 field-gain midpoints. Over S, electrons release $E_{rel} = -\Sigma_S P_e \Delta t = 29.97$ pJ and deuterons gain 1.136 pJ. Unrestricted sums span the full window, $[y]_+ = \max(y, 0)$, and $W_F = W_{pol} + W_{mag}$.

Figure 15 applies this conservation boundary to all negative-electron-work midpoints; each selected midpoint in this scan has positive ion power. Across eleven scales $x = 0.5, 0.6, \ldots, 1.5$, the ratio $f_D = P_D/(-P_e)$ reaches 100% at $P_F = 0$. Below it, electron free-energy release covers ion energy absorption and builds electromagnetic-field energy storage; above it, ions receive energy from both electron free-energy release and electromagnetic-field energy storage. Points A and B on the same $x = 1.5$ trajectory give $f_D = 0.41\%$ and 158.8%, directly exhibiting the two partition states. Both axes contain $-P_e$, so inclined bands also contain a coordinate effect; the directional criterion uses the original power sum $P_D + P_e$.

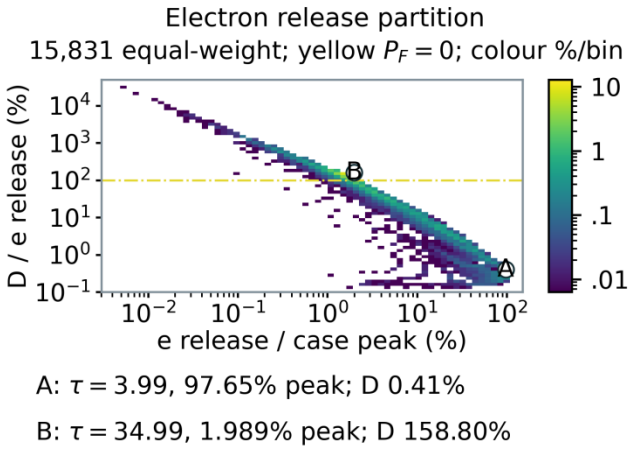


Figure 15 | Conditional distribution of electron free-energy release and simultaneous ion energy absorption. The horizontal axis is $100(-P_e)/\max_t(-P_e)$, normalized within each x trajectory; the vertical axis is $100P_D/(-P_e)$, with logarithmic scales on both axes. Colour gives the percentage of all negative-electron-work time midpoints in each logarithmic bin. The horizontal 100% line marks zero combined electromagnetic-field power; A and B match Figures 14 and 16. Both coordinates contain $-P_e$; direction follows from the original power sum.

Comparison across scales further resolves how electron free-energy release is partitioned relative to field accumulation. From $x = 0.5$ to

1.5, negative-electron-work midpoints increase from **50.45%** to **81.90%** of the full observation window. Within those midpoints, the conditional fraction of field gain falls from **91.77%** to **20.70%**, while the field-supply fraction rises from **8.23%** to **79.30%**. Figure 18 locates the two classes in the time–scale plane: simultaneous ion energy absorption determines field gain or loss during electron free-energy release. The scale dependence also combines changes in gyroaveraging, polarization coefficient, initial free-energy partition and common-field history, describing the full response of this specified family of initial states.

Figure 16 further resolves A and B into powers of electrons, deuteron ions, polarization and magnetic energy storage. At $x = 1.5$ and $\tau = 3.99$, ions receive 0.41% of electron free-energy release and the combined field gains 99.59%. At $\tau = 34.99$, ion energy absorption reaches 158.8% of electron free-energy release, with the combined field supplying 58.80%. Equal and opposite endpoint powers close every exchange edge, with polarization and magnetic energy storage participating simultaneously. Changes in magnetic energy storage follow the phase relation between current and inductive field, so magnetic and polarization energy storage enter the common-field balance together.

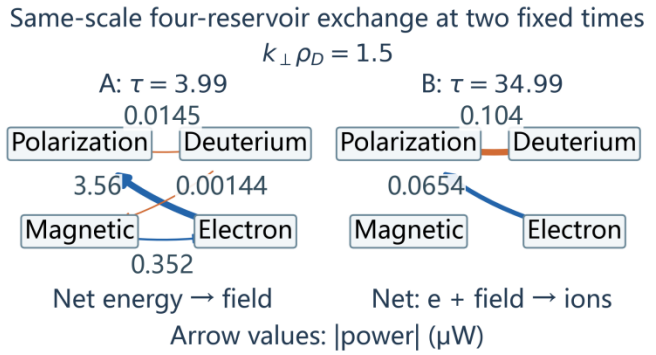


Figure 16 | Instantaneous energy-transfer pathways among the four energy reservoirs at points A and B. Both panels use $x = 1.5$, with A and B at $\tau = 3.99$ and 34.99. Nodes represent electrons, deuteron ions, polarization and magnetic energy storage. Arrows give instantaneous direction in the fixed potential representation; labels give absolute power in microwatts. Endpoint powers on each edge are equal and opposite. Line widths are scaled independently; the drawing threshold is 0.001 microwatts, and net powers use the complete data.

Figure 17 gives the accumulated effect of instantaneous partition. Adding the integrated powers to the initial stored energies gives $W_F = W_{\mathrm{pol}} + W_{\mathrm{mag}}$, W_D and W_e, whose sum is W_0. A trough-to-peak field-energy rise equals integrated electron free-energy release after subtracting simultaneous ion energy absorption; subsequent field-energy loss supplements particle reception. This balance partitions energy storage by field and species, whereas the three-wave balance partitions energy storage by spectral mode, each containing field and particle responses. The full power balances and corresponding stored-energy definitions connect the two partitions.

The electromagnetic field acts as an intermediate energy reservoir during the exchange process, while the relative magnitudes of electron energy release and deuteron ion energy absorption determine the temporal evolution of the stored field energy. Electron supply and ion energy absorption occur simultaneously, and their difference controls field accumulation; polarization and magnetic energy storage together constitute this electromagnetic response. In the present collisionless model, energy absorbed by the deuteron ion population is quantified through the free energy associated with its distribution perturbation. This quantity should not be interpreted as irreversible heating. Irreversible energy conversion is considered separately through the viscous-dissipation model introduced below.

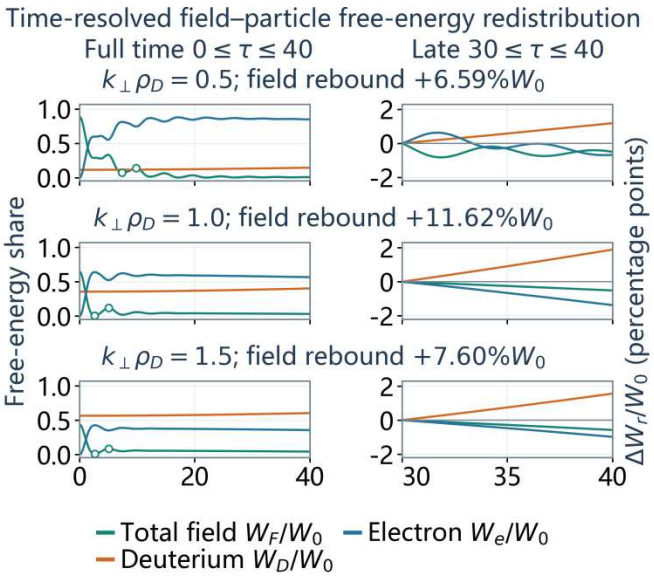


Figure 17 | Stored-energy integrals for the combined field and two thermal species. Rows use $x = k_\perp \rho_D = 0.5, 1.0, 1.5$, with $\tau = k_\parallel v_{\mathrm{th},e} t$ on the abscissa. The left column gives $W_F = W_{\mathrm{pol}} + W_{\mathrm{mag}}$, W_D and W_e divided by each row's W_0; their shares sum to 1. Open circles mark a field-energy trough and subsequent peak, whose endpoints satisfy $P_F = 0$. The right column gives energy storage changes relative to $\tau = 30$, divided by W_0 and multiplied by 100, in percentage points. Each row uses its own initial total.

Figures 18–20 connect this partition and its energy storage changes to integrable signed powers. Green and orange regions in Figure 18 locate field gain and field supply during electron free-energy release; electron-power zero crossings in Figure 19 correspond to electron-storage extrema in Figure 17. Adding Figure 19 pointwise to the ion power in Figure 14 gives $P_D + P_e = -\dot{W}_F$ in Figure 20: positive area is accumulated field-to-particle output, absolute negative area is accumulated return, and their difference is net output. Each row of Figure 17 uses its own W_0, and W_0 differs by about a factor of 10.06 between scale endpoints; absolute energy comparisons multiply each share by its corresponding initial total.

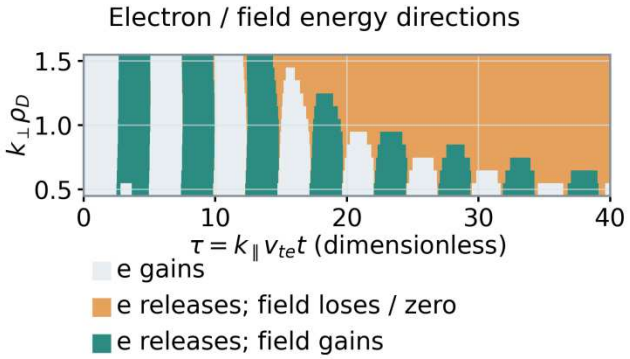


Figure 18 | combined electromagnetic-field power regions during electron free-energy release. The axes are $\tau = k_\parallel v_{\mathrm{th},e} t$ and $x = k_\perp \rho_D$, spanning 0.5–1.5. Green denotes $P_e < 0, P_F > 0$, orange $P_e < 0, P_F < 0$, and grey field-to-electron transfer. The green–orange boundary $P_D = -P_e$ matches the 100% line in Figure 15. Colours indicate instantaneous direction along each scale trajectory; stepped boundaries reflect discrete sampling.

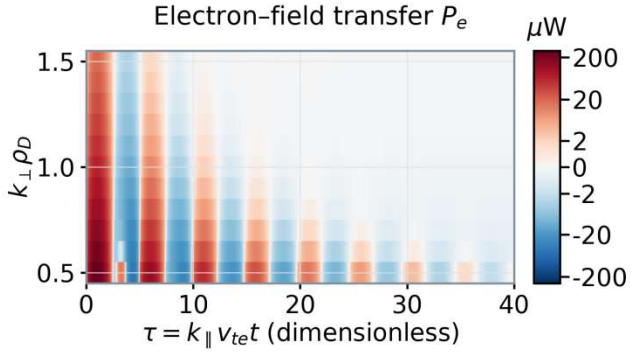


Figure 19 | Instantaneous power from the common electromagnetic field to thermal electrons. The axes are $\tau = k_\parallel v_{\mathrm{th},e} t$ and $x = k_\perp \rho_D$, spanning 0.5–1.5. Colour gives $P_e = (V/2)\mathrm{Re}(E_\parallel j_e^*)$ in microwatts, with $V = 1\,\mathrm{m}^3$. Positive red indicates gain of electron distribution free energy W_e, negative blue electron free-energy release, and white near-zero power. At fixed x, power zero crossings mark local extrema of W_e.

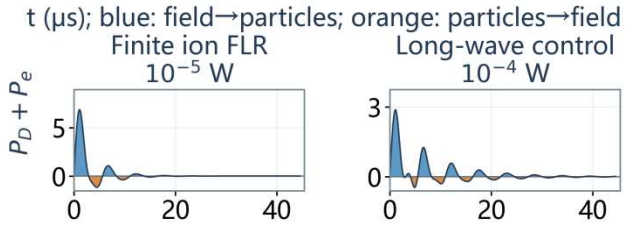


Figure 20 | Combined thermal-species power and rate of change of electromagnetic-field energy. Left and right use $x = k_\perp \rho_D = 1$ and $x = 0.5$; the abscissa is physical time t (μs), and the ordinate is $P_D + P_e = -\dot{W}_F$ (W), with $W_F = W_{\mathrm{pol}} + W_{\mathrm{mag}}$ and reference volume $1\,\mathrm{m}^3$. Positive blue area represents transfer from polarization and magnetic energy storage combined to thermal electrons and deuterium; the absolute negative orange area denotes their net return to the field. The first four orange intervals in the main case are approximately 2.894–5.610, 8.371–11.09, 13.85–16.48 and 19.41–$21.73\,\mu$s. Zero crossings reverse instantaneous direction and mark field-energy extrema; the panels use different vertical scales.

Applying field–species partition to modal stability first requires specifying the energy storage assigned to the coherent mode. For a weakly growing mode with established spatial structure and complex frequency $\omega = \omega_r + \mathrm{i}\gamma$, let W_{mode} be its positive quadratic energy storage; an amplitude varying as $e^{\gamma t}$ has energy rate $2\gamma W_{\mathrm{mode}}$. Taking fast particles as the source, and thermal-particle free energy outside coherent energy storage together with outward regional flux as the receiving terms, gives

$$2\gamma W_{\mathrm{mode}} = P_{\mathrm{EP}\to\mathrm{mode}} - P_{\mathrm{mode}\to\mathrm{thermal}} - \mathcal{F}_{\mathrm{out}}. \qquad (18)$$

Equation (18) expresses the partition mechanism as the stability balance of one coherent mode. Every power uses a common field structure, averaging, volume and normalization; coherent particle response belongs to W_{mode}, and the remaining thermal-particle reception belongs to the corresponding output term. Additional intermodal channels enter the selected-mode balance and cancel pairwise in the full modal system. The local calculation establishes how $P_D + P_e$ controls field–species partition. Applying this mechanism to the global candidate requires evaluating each power with that mode's field structure and a common initial state, so that the net balance determines growth or damping.

Electron-Beam-Driven Electrostatic Field Excitation and Distribution Evolution

The preceding calculation examines energy exchange between thermal species and a self-consistent electromagnetic field. To investigate a distinct mechanism of electron-driven field excitation, we next consider an independent electrostatic beam – plasma model. This calculation isolates the contribution of beam drift energy and the subsequent redistribution of energy between beam electrons, background electrons, and the electric field. Using reduced time $\tau = \omega_p t$, where ω_p is the reference plasma angular frequency, and normalizing length by $v_{\mathrm{ref}}/\omega_p$ gives the Vlasov–Poisson system

$$\partial_\tau f_s + v\,\partial_x f_s - E\,\partial_v f_s = 0,$$
$$\partial_x E = 1 - \sum_s \int f_s \,\mathrm{d}v,$$
$$s \in \{\mathrm{background}, \mathrm{beam}\}. \qquad (19)$$

Spatial advection changes particle phase relative to the field, while the electric term changes electron velocity, coupling distribution evolution back to the field. The plotted τ is physical time multiplied by the reference plasma angular frequency; 2π corresponds to one reference oscillation period. This electron-timescale benchmark compares drift energy release with distribution rearrangement under independently specified parameters. Dots in equation (20) denote derivatives with respect to reduced time.

The direction of energy transfer follows from the second velocity moment of equation (19). Defining $K_s = \iint v^2 f_s/2 \,\mathrm{d}v\,\mathrm{d}x$ and $U_E = \int E^2/2 \,\mathrm{d}x$, periodic space and zero velocity-boundary flux eliminate boundary terms, giving

$$\dot{K}_s = P_s^{\mathrm{beam}} = -\iint v E f_s \,\mathrm{d}v\,\mathrm{d}x,$$
$$\dot{U}_E = -\sum_s P_s^{\mathrm{beam}}. \qquad (20)$$

Equation (20) places beam-drift loss, background-electron reception and field growth in one energy balance. The numerical solution reveals gives the first maximum of the fundamental electric-field amplitude in Figure 21 at $\tau = 27$, with amplitude 0.4979, followed by decline and repeated oscillation; the coarse-grid peak is 0.4901, about 1.57% lower. Figure 22 further shows that early beam-energy loss accompanies simultaneous gains by background electrons and the field, followed by partial beam-energy recovery. The subsequent evolution of the electric-field amplitude reflects competing energy-transfer processes, including electron-to-field energy transfer and partial reverse energy transfer. Their relative contributions are quantified using the time-integrated species-resolved power balances.

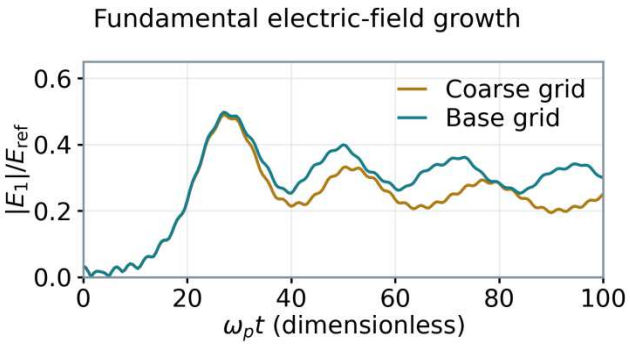


Figure 21 | Fundamental-field amplitude driven by the electron beam. The abscissa is τ and the ordinate is fundamental electric-field Fourier amplitude divided by E_{ref}. The cyan curve uses 65 spatial points, 256 velocity points and $\Delta\tau = 0.01$; the ochre curve uses 33, 128 and 0.02. Curves display the first peak and subsequent oscillation, with the two grid trajectories gradually separating later; 2π corresponds to one reference plasma-oscillation period.

By $\tau = 32$, beam kinetic energy in Figure 22 has decreased by 9.711 normalized units, while background electrons and field have gained 8.730 and 0.948; by 41.5, beam energy has recovered 3.623, or 37.3% of its previous decrease. Maximum relative drift of the three-reservoir total is 0.193%. Together these quantities support a sequence of strong early electron free-energy release, field excitation and subsequent partial return. Later oscillations moderate while exchange continues, with field energy still above its initial value at $\tau = 100$. This collisionless beam example and the preceding thermal-deuteron ion example isolate initial supply and common-field partition, respectively. wave-partical energy exchange connects their mechanisms, while each retains its own initial state, species and normalization.

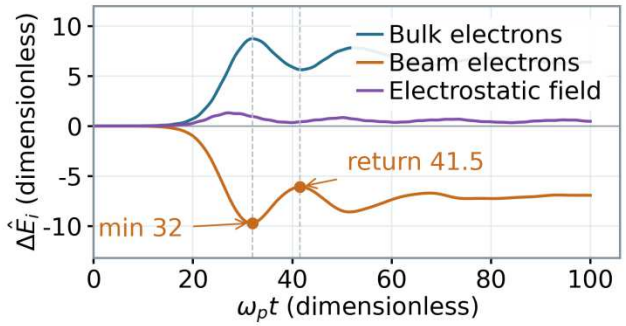


Figure 22 | Energy changes of background electrons, beam electrons and electric field. The abscissa is τ and the ordinate is $\Delta\hat{E}_j = [E_j(t) - E_j(0)]/(n_{\mathrm{ref}}T_{\mathrm{ref}}L_{\mathrm{ref}})$, normalized per transverse area. Blue, orange and purple denote background-electron kinetic, beam-electron kinetic and electrostatic-field energies. Positive and negative values indicate gains and losses relative to the initial state; slopes give reduced component powers in this energy normalization.

Wave-Stress-Driven Axisymmetric MHD Response

Energy exchange between particles and fields also has spatial structure: wave momentum stress drives flow, which changes magnetic field and pressure through ideal induction and adiabatic compression. Figures 23–25 resolve these responses in an independent axisymmetric ideal-MHD receiving system, evolved from zero displacement and velocity under the prescribed cycle-averaged stress $\mathbf{F}_0$ of a prescribed, time-independent wave-field configuration. Wave–particle interactions can also produce macroscopic plasma responses through the transfer of momentum from wave fields to the background plasma. In the present calculation, Figures 23–25 examine the axisymmetric ideal-MHD response to a prescribed cycle-averaged stress associated with a prescribed, time-independent wave-field configuration. The resulting momentum transfer drives plasma flow and induces corresponding magnetic-field and pressure perturbations through ideal induction and adiabatic compression. The imposed stress acts as an external forcing term in this reduced receiving-system model, rather than being dynamically coupled to the evolving wave field. Equilibrium quantities carry subscript zero, with $\mathbf{J}_0 = \nabla \times \mathbf{B}_0/\mu_0$; $\mathbf{U} = \partial_t \boldsymbol{\xi}$ is flow velocity, $\mathbf{J}_1 = \nabla \times \mathbf{b}_1/\mu_0$ perturbed current and Γ the adiabatic index. Linear ideal MHD gives

$$\rho_0 \ddot{\boldsymbol{\xi}} = \mathbf{J}_1 \times \mathbf{B}_0 + \mathbf{J}_0 \times \mathbf{b}_1 - \nabla p_1 + \mathbf{F}_0,$$
$$\mathbf{b}_1 = \nabla \times (\boldsymbol{\xi} \times \mathbf{B}_0),$$
$$p_1 = -\Gamma p_0 \nabla \cdot \boldsymbol{\xi} - \boldsymbol{\xi} \cdot \nabla p_0,$$
$$\sigma = \sqrt{2S:S},$$
$$S = 1/2\,[\nabla \mathbf{U} + (\nabla \mathbf{U})^T]. \quad (21)$$

Equation (21) supplies three connected observables. At $t = 112.8\,\mu$s, the outer bright region at $s \gtrsim 0.8$ in Figure 23 shows stronger local gradients of the forced flow, with a saved-grid maximum strain rate of $0.2640\,\mathrm{s}^{-1}$. The same displacement produces the signed magnetic perturbations in Figure 24 through ideal induction, with maximum vector magnitude 1.144×10^{-10} T. Adiabatic compression and background-pressure advection produce the pressure patches in Figure 25, with maximum absolute value 3.232×10^{-6} Pa. Together the figures show how prescribed wave stress organizes spatial flow, magnetic and pressure responses in the receiving plasma; their amplitudes follow this forced model's energy normalization.

Current is associated with the curl of magnetic perturbation, pressure responds through compression and advection, and strain rate measures velocity gradients. These quantities connect wave-partical energy exchange to receiving-mode geometry. This example uses ideal MHD, with energy storage changes governed by prescribed-force work and ideal restoring response. With viscous stress included, velocity gradients enter dissipative power; the independent continuum model below quantifies heat reception on that basis.

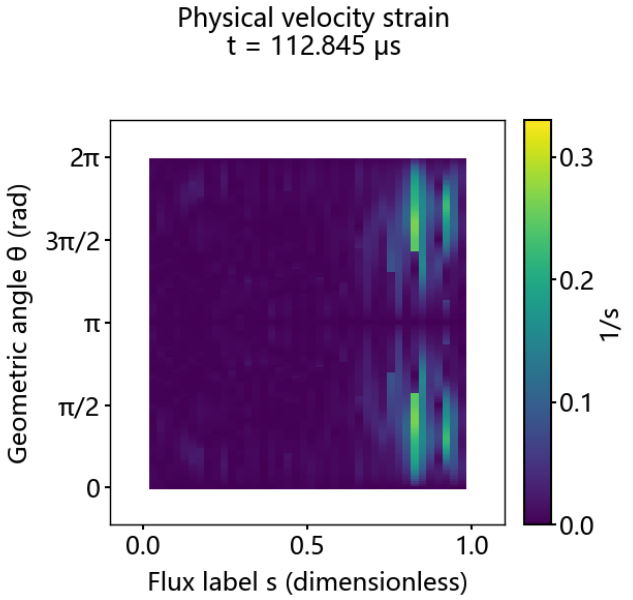


Figure 23 | Strain rate of the forced axisymmetric velocity field. The abscissa is dimensionless flux label s and the ordinate geometric poloidal angle θ (rad, 0–2π). At $t = 112.8\,\mu$s, colour gives the nonnegative strain rate $\sigma = \sqrt{2S:S}$ (s^{-1}) from Eq. (21), including shear and compression; brighter colours indicate larger local velocity gradients.

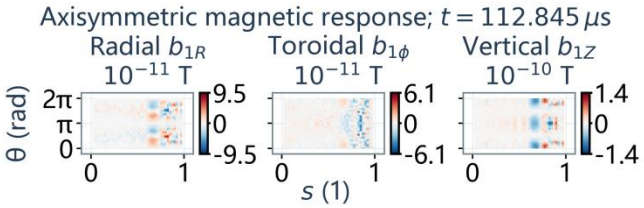


Figure 24 | Forced axisymmetric magnetic-field perturbation. The abscissa is dimensionless flux label s and the ordinate geometric poloidal angle θ (rad). At $t = 112.8\,\mu$s, panels show $b_{1R}, b_{1\varphi}, b_{1Z}$ (T) from left to right. Red is positive, blue negative and white near zero; each panel uses its own symmetric colour scale.

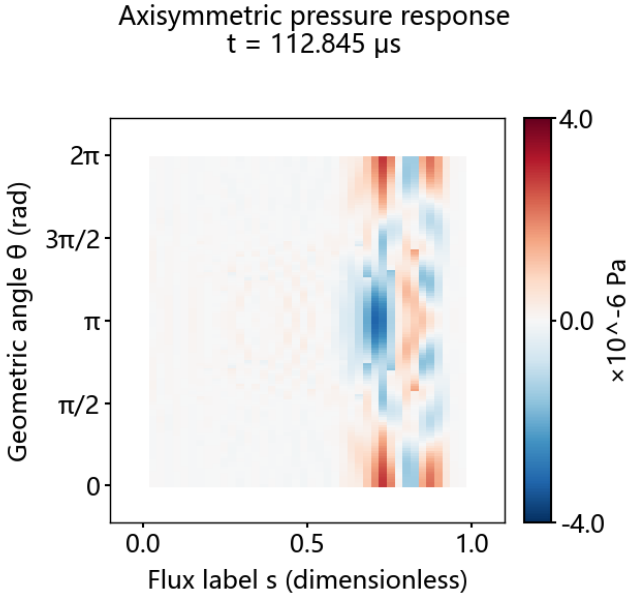


Figure 25 | Forced axisymmetric pressure response. The abscissa is dimensionless flux label s and the ordinate geometric poloidal angle θ (rad). At $t = 112.8\,\mu$s, colour gives pressure perturbation p_1 (Pa): red is positive, blue

negative and white near zero, indicating local changes relative to equilibrium pressure.

At the time shown in Figures 23–25 (112.845 μs), the local mechanical-power density is $\mathbf{U} \cdot \mathbf{F}_0$, where $\mathbf{U}$ is the receiving plasma's velocity and $\mathbf{F}_0$ is the force density exerted by the prescribed wave stress in Eq. (21). Figure 26 shows adjacent regions of positive and negative work near the plasma edge. Integrated over the toroidal volume, these regions contribute +40.41 and −32.20 nW, respectively, leaving a net input of 8.21 nW.

From rest to this time, the stress delivered 0.2662 pJ of work. The receiving plasma stored 0.1946 pJ (73.1%) as kinetic energy and 0.07164 pJ as ideal-MHD restoring potential energy. The energy flux through the fixed wall was zero. This balance measures mechanical energy supplied to the plasma. Quantifying parent-wave depletion or irreversible heating would require additional diagnostics.

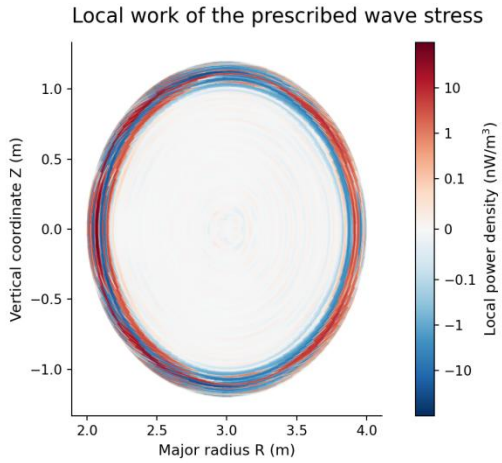


Figure 26 | Local power density of the prescribed wave stress. Red marks work done on the plasma and blue marks work returned to the forcing in the poloidal cross-section. The colour scale is in nW m^{-3} and is linear within ±0.1 nW m^{-3}.

Orbit selection, resonant trapping and distribution evolution

Particle-orbit sampling of the wave field provides an additional mechanism governing resonant wave – particle energy exchange. Guiding centres in a static equilibrium follow Hamiltonian H_0, where $p_\parallel = m_D v_\parallel$ and B_{eq} is equilibrium magnetic-field strength. For conserved magnetic moment, μB_{eq} increases in high-field regions, producing mirror reflection when parallel kinetic energy reaches zero; particles retaining sufficient parallel energy complete a poloidal transit. The zero-probe calculation in Figure 27 exhibits both motions, with population median orbit width 0.164 m and maximum 0.783 m, showing that orbit sampling spans a finite radial range. To measure phase matching between this sampling and a prescribed field, let $h_{1i}(t)$ be the complex first-order vector-potential interaction amplitude along an orbit and define the particle-weighted orbit-field coupling spectrum

$$H_0(\mathbf{X}, p_\parallel, \mu) = \frac{p_\parallel^2}{2m_D} + \mu B_{\mathrm{eq}}(\mathbf{X}),$$

$$C_i(f) = \frac{1}{T}\int_0^T h_{1i}(t) e^{-2\pi i f t}\, \mathrm{d}t,$$

$$S(f) = \sum_i w_i \, |C_i(f)|^2,$$

$$\hat{S}(f) = \frac{S(f)}{\max_{f \in \mathcal{F}} S(f)}. \quad (22)$$

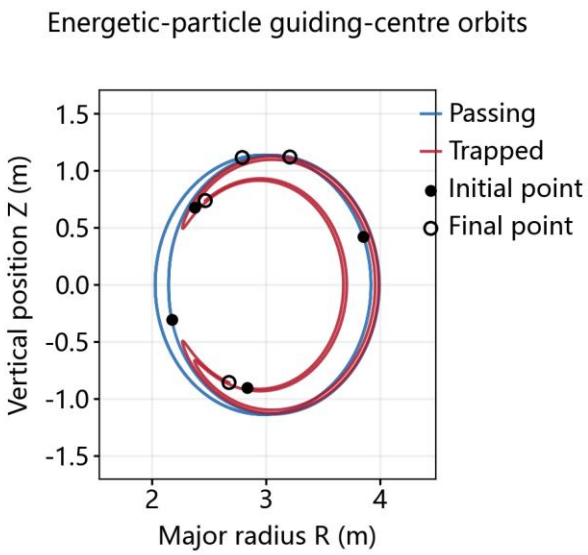


Figure 27 | Passing and mirror-trapped zero-probe guiding-centre orbits. The axes are R and Z (m). Over the $60\,\mu$s window, blue trajectories have at least 2π net poloidal transit; red trajectories reverse $p_\parallel$ and have net transit below 2π. Filled and open circles mark initial and final states. Four trajectories are selected by spatial span from the 2048-particle population. Classification uses real-space guiding-centre motion in the static magnetic field.

In Eq. (22), $T = 60\,\mu$s, w_i is physical-particle-number weight and $\mathcal{F}$ the probe-frequency set. The nonnegative particle-number-weighted squared energy S measures finite-window occupied coupling between the specified population and prescribed field shape. For 8192 zero-probe orbits, Figure 28 plots peak-normalized $\hat{S}$ and gives a coupling peak near 78 kHz, jointly selected by orbit phases, population occupancy and the prescribed $n = 2, m = 5$ field. The $60\,\mu$s window supplies a resolution scale of 16.67 kHz, and the displayed band contains 7.33% of physical particle weight. This frequency interval identifies candidate resonant components for subsequent analyses of phase-dependent particle work and resonant wave – particle interactions. The calculated spectrum quantifies the finite-time coupling strength between the prescribed wave-field structure and the sampled particle population. It provides a diagnostic of potentially important orbit–field frequency matching, rather than a direct measurement of absorbed wave power or resonant particle transport. Establishing the actual energy-transfer rate requires evaluating the phase-dependent particle work along the corresponding trajectories. Growth rate follows from a common modal power balance; island width and bounce frequency follow from local Hamiltonian curvature and coupling amplitude. A global-response component near 80.42 kHz is numerically close to this band and varies with the representation basis; the two quantities retain their respective definitions as a global-response component and a prescribed-field occupied coupling peak.

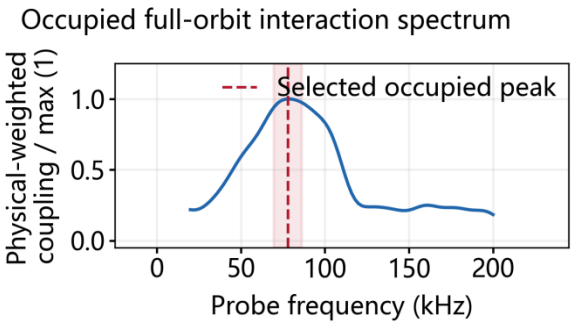


Figure 28 | Finite-time particle-weighted coupling spectrum for the prescribed wave field. The abscissa spans 20–200 kHz in 2 kHz steps; the ordinate is the peak-normalized spectrum $\hat{S}$ from Eq. (22). The spectrum sums squared Fourier amplitudes of first-order interaction along 8192 zero-probe orbits, weighted by physical particle number. The prescribed field has $n = 2, m = 5$ and a radial envelope centred on the $q_{\min}$ surface. The integration

window is $60\,\mu$s; the shaded half-width of 8.333 kHz is half a window-resolution scale.

In addition to magnetic-mirror trapping, a finite wave can trap particles in resonant phase. To display this topology, we first transform to canonical coordinates rotating with the resonant wave phase and then expand about the resonant action P_{res}. The resonance condition removes the linear action term. Retaining positive curvature $\alpha > 0$ and a single-harmonic coupling amplitude $U > 0$ gives the pendulum normal form. Here θ is resonant phase, P its conjugate action, I normalized action and τ time normalized by the small-amplitude bounce angular frequency $\sqrt{\alpha U}$:

$$H - H_{\mathrm{ref}} = \frac{\alpha}{2}(P - P_{\mathrm{res}})^2 - U\cos\theta,$$

$$I = (P - P_{\mathrm{res}})\sqrt{\frac{\alpha}{U}},$$

$$\tau = t\sqrt{\alpha U},$$

$$K = \frac{H - H_{\mathrm{ref}}}{U} = \frac{I^2}{2} - \cos\theta \quad (23)$$

Hamilton's equations give $\mathrm{d}\theta/\mathrm{d}\tau = I$ and $\mathrm{d}I/\mathrm{d}\tau = -\sin\theta$. The unstable fixed points $\theta = \pm\pi, I = 0$ have $K = 1$, yielding the separatrix $I_{\mathrm{sep}} = \pm 2\cos(\theta/2)$, whose action half-width at $\theta = 0$ is 2. Numerical trajectories in Figure 29 verify this topology: four closed blue orbits satisfy $K < 1$ and oscillate about the prescribed wave phase, while two orange orbits satisfy $K > 1$ and circulate in phase. Close to the separatrix, particles spend longer near the saddle, making the bounce period more sensitive to action. Trapping here means canonical phase locking in a prescribed single resonance; trapping in Figure 27 means mirror reflection in the static field. A quantitative comparison of these two trapping mechanisms requires mapping the corresponding orbit and resonance classifications onto a common particle population, equilibrium configuration, and wave field.

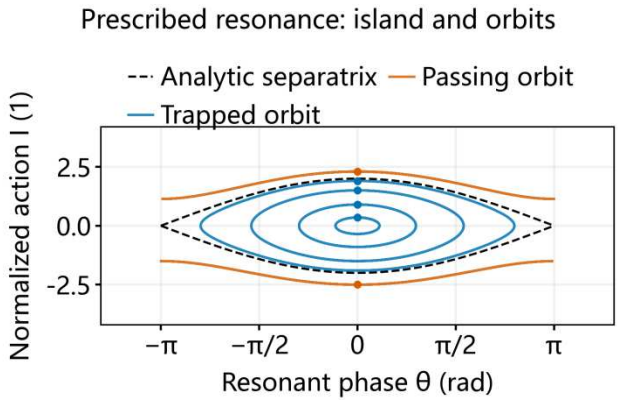


Figure 29 | Resonant phase-space island and passing trajectories in the prescribed single-resonance model. The horizontal axis is resonant phase θ (rad, $-\pi$ to π), and the vertical axis is dimensionless canonical action I. The black dashed curve is the analytic separatrix $K = 1$; blue curves show four trapped trajectories with $K < 1$, orange curves show two passing trajectories with $K > 1$, and dots mark initial states. At $\theta = 0$, the maximum action half-width is 2. Closed and circulating trajectories distinguish phase locking from passage in the prescribed wave; action and time use local normalizations.

Variation of orbital angular frequency with action also shears a distribution of finite width into filaments. Phase-space continuity and the zero divergence of Hamiltonian flow give the collisionless transport equation, where $\Phi_{-\tau}$ maps a point backward along its characteristic to the initial state. The distribution f is probability density per radian of phase and unit normalized action, with its value preserved along each characteristic:

$$\partial_\tau f + I\,\partial_\theta f - \sin\theta\,\partial_I f = 0,$$

$$f(\theta, I, \tau) = f_0(\Phi_{-\tau}(\theta, I)) \quad (24)$$

Figure 30 reconstructs the distribution evolution in Eq. (24) using backward characteristics. The initial state has compact support in $I \in [-0.4, 1.8]$. By $\tau = 4$ and 8, orbital-frequency differences inside the island and near the separatrix stretch and fold the high-value band into filaments. This morphological evolution is consistent with preservation of distribution values along characteristics and of integrated probability under the continuous Hamiltonian flow. The figure thus establishes rearrangement of the distribution in phase space by conservative resonant dynamics. The energetic meaning of thermalization is defined by collisions or another stated irreversible receiving mechanism and its power balance.

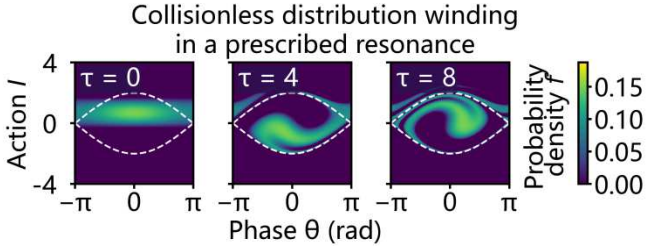


Figure 30 | Collisionless winding of a probability density in the prescribed single resonance. The panels correspond to reduced times $\tau = 0, 4, 8$; the horizontal axis is resonant phase θ (rad, $-\pi$ to π), and the vertical axis is dimensionless action I. The common colour scale is probability density f per radian and unit normalized action; white dashed lines show the same analytic separatrix $K = 1$ as in Figure 29. The initial band is sheared along trapped and passing trajectories, forming filaments within the island and near the separatrix; its integrated probability is conserved by the collisionless Hamiltonian flow.

Figures 31–33 connect this phase-space mechanism to the preceding self-consistent beam evolution, using reduced time $\tau = \omega_p t$, where ω_p is the reference plasma angular frequency. The initial high-value band in Figure 31 lies near $v/v_{\mathrm{ref}} \simeq 4.5$, with a 1% periodic perturbation supplying initial phase structure for the field feedback in Eq. (19). After the first field peak, Figure 32 at $\tau = 50$ exhibits phase-space structures characteristic of resonant trapping and filamentation as the high-value band winds around low-density cores; Figure 33 at $\tau = 100$ shows a wider region and finer alternating structures. The maximum grid value decreases from 0.08039 to 0.06442 and 0.03416, the latter two being 80.1% and 42.5% of the initial peak. These quantities describe finite-grid peak heights and distribution rearrangement; particle number is measured by phase-space integration and energy direction by the species powers in Eq. (20). Together with sustained oscillation and partial return in Figures 21–22, they connect field-amplitude evolution to feedback involving redistribution in phase space. Quantitative late-time filament scales depend on phase-space resolution.

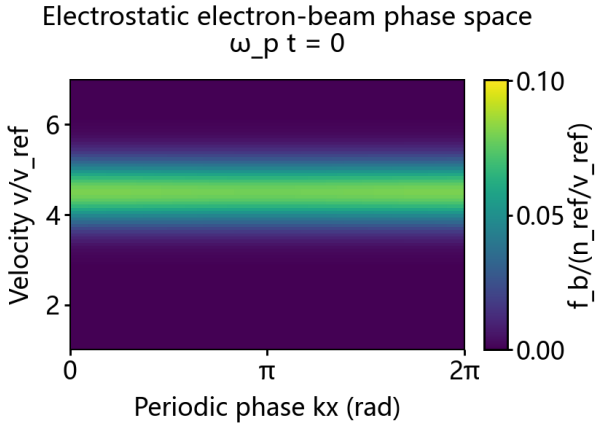


Figure 31 | Initial beam-electron phase–velocity state at $\tau = 0$. The abscissa is periodic phase kx (rad, 0–2π), and the ordinate is v/v_{ref}, displayed over 1–7. Colour gives the nonnegative beam distribution $f_b/(n_{\mathrm{ref}}/v_{\mathrm{ref}})$ on a 0–0.1005 scale. Figures 31–33 share this display range and colour scale. Time is normalized by the reference plasma angular frequency; 2π is one reference oscillation period.

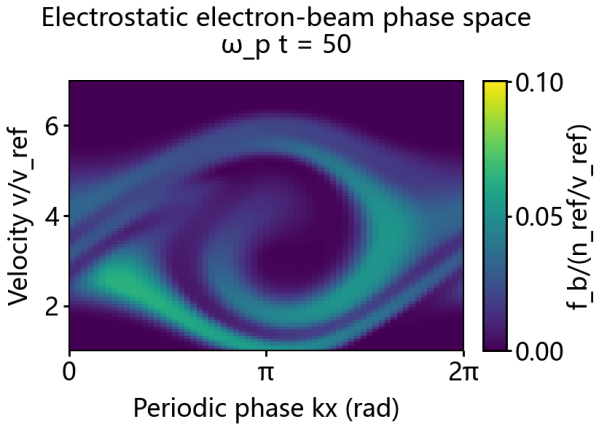


Figure 32 | Beam-electron phase–velocity distribution at $\tau = 50$. The axes are $kx \in [0,2\pi]$ (rad) and $v/v_{\mathrm{ref}} \in [1,7]$. Colour represents $f_b/(n_{\mathrm{ref}}/v_{\mathrm{ref}})$ on the scale shared with Figure 31. This state follows the first maximum of the fundamental electric-field amplitude.

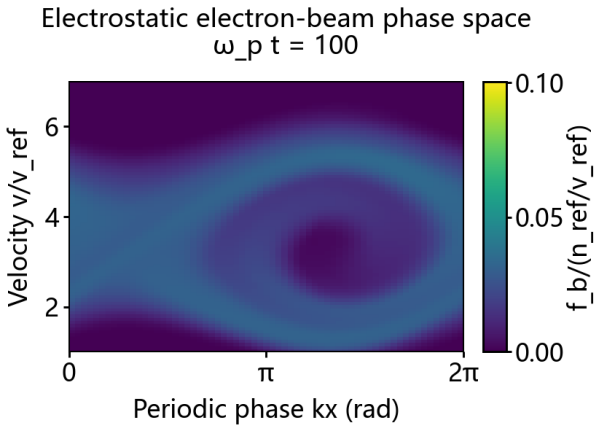


Figure 33 | Beam-electron phase–velocity distribution at $\tau = 100$. Phase kx, velocity v/v_{ref} and distribution $f_b/(n_{\mathrm{ref}}/v_{\mathrm{ref}})$ use the display ranges and colour scale of Figures 31–32. This final state corresponds to the same time in Figures 21–22, allowing joint comparison of distribution morphology, fundamental amplitude and component energies.

Phase mixing and energy dissipation

Spatially varying wave frequencies can produce phase mixing, leading to a progressive reduction in the coherent wave response across neighbouring magnetic surfaces. Figures 34–35 isolate this mechanism with the ideal shear continuum on independent magnetic surfaces: neighbouring surfaces have different branch frequencies $\omega_j(s)$, and each branch retains its energy while accumulating phase. Let $E_j(s) \geq 0$ be initial branch energy and $w_s > 0$ the radial quadrature weight, with total initial energy $E_0 = \sum_{s,j} w_s E_j(s)$. Defining coherence by energy-inner-product projection onto the initial direction gives

$$a_j(s,t) = a_j(s,0)e^{-i\omega_j(s)t},$$

$$C(t) = E_0^{-1} \sum_{s,j} w_s E_j(s) e^{-i\omega_j(s)t},$$

$$W_{\mathrm{coh}} = E_0 |C|^2,$$

$$W_{\mathrm{orth}} = E_0 - W_{\mathrm{coh}}. \quad (25)$$

Equation (25) combines local energy retention and global coherence loss in one propagation law: frequency differences progressively cancel complex phases in the projected sum. The smooth shear displacement at $t = 0$ in Figure 34 supplies the initially coherent structure; dense radial bands at $t = 0.8$ ms in Figure 35 reveal the growing phase gradient. The numerical solution reveals partitions the initial 1 J into coherent energy 0.05029 J (5.03%) and orthogonal energy 0.9497 J (94.97%), with coherent amplitude about 22.42% of its initial value. The total ideal-wave energy remains conserved, while the decrease in coherent-mode energy is accompanied by a corresponding increase in energy associated with orthogonal wave structures. Phase mixing also strengthens radial gradients, providing scales on which gradient-dependent dissipation can act.

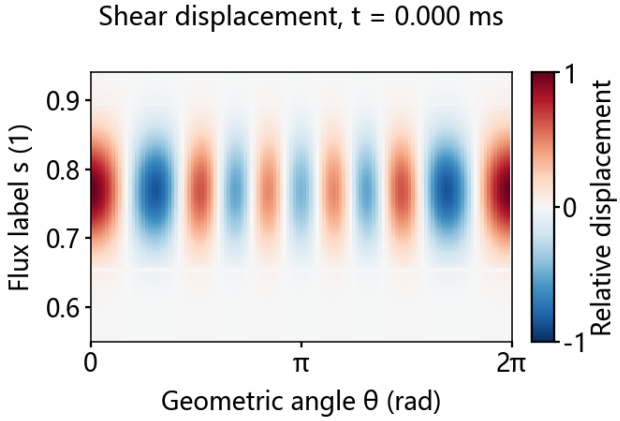


Figure 34 | Continuum shear displacement at $t = 0$. The abscissa is geometric poloidal angle θ (rad, 0–2π) and the ordinate dimensionless flux label s (approximately 0.55 – 0.94). Colour gives the real tangential shear displacement divided by a common reference maximum absolute amplitude, using the dimensionless $[-1,1]$ scale shared with Figure 35. Red is positive, blue negative and white near zero.

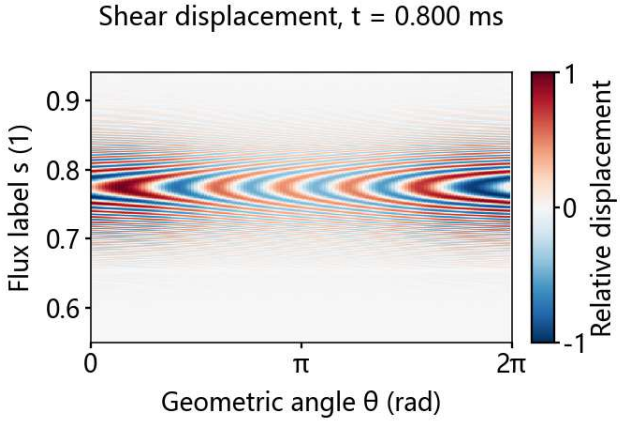


Figure 35 | Continuum shear displacement at $t = 0.8$ ms. The abscissa is geometric poloidal angle θ (rad) and the ordinate flux label s. Colour gives the real tangential shear displacement with the common reference amplitude and dimensionless $[-1,1]$ scale of Figure 34. Radial spacing between adjacent red and blue bands reflects the local phase gradient.

To connect these gradients to irreversible reception, Figures 36–37 add prescribed scalar viscosity to the same low-frequency continuum input. The single-branch reduction retains radial variation of the three-component shear basis and represents viscous stress by a positive-semidefinite matrix D in the high-radial-gradient approximation. Natural zero radial traction gives zero viscous boundary work. With $\boldsymbol{\eta}$ and $\mathbf{v}$ denoting modal displacement and velocity, taking the energy inner product of the motion equation with velocity yields a balance equating wave-energy loss to nonnegative viscous dissipation:

$$M\dot{\mathbf{v}} + K\boldsymbol{\eta} + \nu D\mathbf{v} = 0,$$

$$\dot{\boldsymbol{\eta}} = \mathbf{v},$$

$$W = 1/2\,(\mathbf{v}^{\dagger}M\mathbf{v} + \boldsymbol{\eta}^{\dagger}K\boldsymbol{\eta}),$$

$$\dot{Q}_{\nu} = \nu\mathbf{v}^{\dagger}D\mathbf{v} \geq 0,$$

$$\frac{\mathrm{d}}{\mathrm{d}t}(W + Q_{\nu}) = 0. \quad (26)$$

Here $M = M^{\dagger} > 0$, $K = K^{\dagger} \geq 0$, $D = D^{\dagger} \geq 0$ and $\nu \geq 0$. The stable modal subspace gives positive wave energy, with factor $1/2$ supplied by this example's modal-coordinate normalization. For state $y = (\boldsymbol{\eta}, \mathbf{v})$, the energy inner product satisfies $\langle y, y\rangle_E = W$, so coherent energy with dissipation is $W_{\mathrm{coh}} = |\langle y_0, y(t)\rangle_E|^2 / \langle y_0, y_0\rangle_E$

and orthogonal wave energy is $W_{\mathrm{orth}}(t) = W(t) - W_{\mathrm{coh}}(t)$. In the zero-viscosity control of Figure 36, coherent energy decreases and orthogonal energy rises while total wave energy is retained. Introducing a positive viscosity produces cumulative irreversible energy dissipation, which is accounted for through the viscous-work integral: Q_ν rises and remaining wave energy falls, while wave energy plus heat remains the initial 1 J. At 0.8 ms, $\nu = 0.002,0.01,0.05\,\mathrm{m^2/s}$ converts 46.74%, 73.37% and 88.62% of the initial energy into effective viscous heat. Figure 37 locates reception for $\nu = 0.01\,\mathrm{m^2/s}$ near $s \approx 0.75$ and 0.8. At $t = 0.8$ ms, the local peak is 10.01 J per unit s at $s = 0.7522$; radial integration gives 0.7337 J, matching accumulated heat in Figure 36, with remaining wave energy 0.2663 J. Spatial gradients, nonnegative dissipative work and global wave-energy loss thus correspond within one balance.

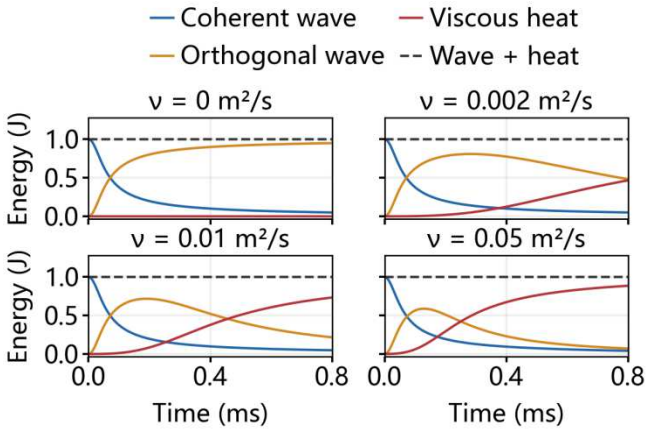


Figure 36 | Evolution of coherent and orthogonal wave energies and cumulative viscous dissipation. Axes are physical time t (ms, 0–0.8) and energy (J); panels use kinematic viscosities $\nu = 0,0.002,0.01,0.05\,\mathrm{m^2/s}$ in sequence. Blue gives coherent-wave energy, orange resolved-wave energy orthogonal to it, red cumulative effective viscous heat Q_ν, and black dashed the sum of wave energy and heat. The red-curve slope gives instantaneous viscous dissipation power in Eq. (26).

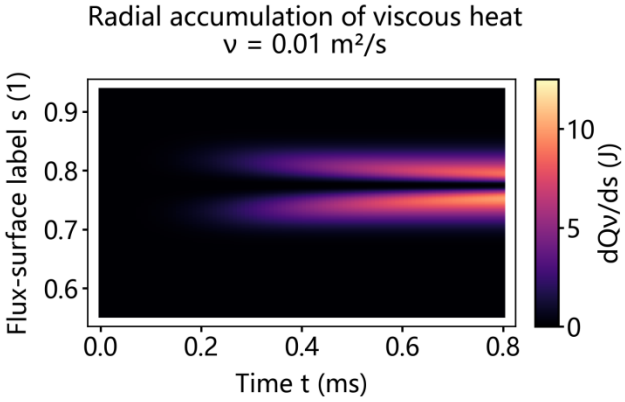


Figure 37 | Radial cumulative viscous heat at $\nu = 0.01\,\mathrm{m^2/s}$. The abscissa is physical time t (ms, 0–0.8), and the ordinate dimensionless flux label s at neighbouring-surface midpoints. Colour gives accumulated edge heat divided by surface spacing Δs, in J per unit s. Integration over s gives cumulative heat; the time slope of a colour value gives local dissipation power per unit s.

These calculations illustrate three distinct energy-transfer mechanisms: redistribution of coherent wave energy through phase mixing, exchange of free energy between thermal species and electromagnetic fields, and irreversible conversion of wave energy into heat through viscous dissipation. The viscous example uses a specified scalar transport coefficient and a fixed thermal background, establishing energy transfer within that effective dissipation model. Applying these processes to RSAE stability under sustained drive entails comparing net supply, particle reception and energy outflow in a common mode through Eq. (18), while following distribution feedback on the drive. The sign and temporal persistence of the net power balance, evaluated together with the evolving particle distributions and radial energy fluxes, provide the criteria for distinguishing mode growth, nonlinear saturation, and decay.

Implications for fusion research and physics-informed inverse co-design framework

These examples separate the RSAE energy problem into testable physical steps: phase determines the direction of intermode transfer, electron free-energy release and deuteron ion reception jointly determine electromagnetic-field energy storage, and distribution rearrangement and dissipation affect whether energy can return to the wave. The central implication is that assessing effective instability suppression under reversed shear requires tracking energy-transfer pathways together with spectral and amplitude evolution. For fusion operation, the corresponding objectives are net deposition into the intended species and fast-ion confinement; modal phases, species powers, irreversible heating and particle loss must enter that assessment together.

Applying this energy criterion to fast-ion-driven RSAE saturation requires kinetic simulations that evolve particle distributions and wave fields together [1,2]. A 6D full-orbit kinetic description evolves $f_h(\mathbf{x}, \mathbf{v}, t)$ in three position and three velocity coordinates, resolving full orbits and gyrophase. A 5D gyrokinetic description evolves $F_h(\mathbf{R}, v_\parallel, \mu, t)$, averaging the fast gyrophase under low-frequency ordering while retaining finite-Larmor-radius, polarization and magnetization contributions at the corresponding order [15]. Time is an independent evolution parameter in both descriptions. The kinetic description should follow resonant trapping, distribution-gradient rearrangement and radial flux while resolving signed powers between electrons, deuteron ions and fields and their back-reaction on mode evolution; model selection and coupling should follow the frequency and spatial scales and the reduction error. The separate mechanism results thereby define verification quantities for self-consistent RSAE kinetic coupling: signed species powers, electromagnetic-field energy storage, distribution rearrangement and particle flux should satisfy consistent energy and particle balances within a common equilibrium and energy normalization.

These physical quantities also specify what AI state estimation must retain. Hu et al. demonstrated Alfvén-activity feedback control by adjusting neutral-beam power using mode amplitudes measured by electron cyclotron emission [18]. Rothstein et al. subsequently used machine-learning observers for mode identification and neutron-deficit estimation in initial neutral-beam-power feedback experiments [19]. In the energy description developed here, state estimates should combine modal amplitudes and phases with resonant occupancy, distribution gradients and particle fluxes, together with peak frequencies and amplitudes. Physics-constrained neural operators could approximate the mapping from initial distributions, compatible initial fields, equilibria, source histories and boundary conditions to distribution–field evolution. Kinetic calculations can supply corresponding distributions, fields and synthetic diagnostic signals for training and testing. The adequacy of an estimate should be tested through the signed powers and fluxes it reproduces; diagnostic degeneracy is represented by uncertainty over the compatible states.

Physics-informed inverse co-design framework can then be posed in terms of achievable fusion objectives: choosing equilibrium profiles, particle-source deposition, diagnostic placement and actuator timing jointly to improve fast-ion retention and energy deposition under operational constraints. Machine-learning models can be used to screen candidate operating configurations, while high-fidelity kinetic simulations provide the physical validation of their effects on resonant particle populations, species-resolved energy transfer, and energetic-particle confinement. The relevant measures include net power delivered to the intended species, fast-ion loss flux and persistence of the saturated state. Consequently optimization objective is to maintain effective energetic-particle deposition while mitigating undesirable Alfvénic activity. Diagnostic configurations and actuator strategies can then be evaluated according to their

measurable effects on energy deposition, particle transport, and mode stability. The energy relations among electron-driven field excitation, electromagnetic-field energy storage, ion energy absorption and dissipation provide testable physical constraints for confinement-oriented design and explain why the required simulations must resolve mode structure, distribution evolution and energy balances together.

Conclusions

This study has investigated complementary mechanisms governing coherent energy transfer and wave–particle energy exchange in reversed-shear Alfvénic systems through a hierarchy of global and reduced theoretical and numerical models.

The conservative three-wave analysis demonstrates that the initial relative phase governs the direction of intermode energy transfer, while the Manley–Rowe invariants and interaction Hamiltonian constrain the accessible energy-exchange trajectories. The frequency-splitting analysis further shows how energy can be redistributed between directly driven and orthogonal daughter-mode combinations.

The local gyroaveraged thermal-species model resolves the temporal partition of free energy between electrons, deuteron ions, and electromagnetic-field reservoirs. The results highlight the importance of species-dependent response times, current–field phase relationships, and polarization and magnetic energy storage in determining the instantaneous and integrated energy balance. An independent electrostatic beam–plasma calculation illustrates the relationship between electron drift-energy release, electric-field excitation, and subsequent reverse energy transfer.

Additional reduced models characterize particle-orbit sampling, resonant phase-space trapping, collisionless distribution rearrangement, continuum phase mixing, and effective viscous dissipation. These calculations distinguish conservative redistribution of resolved wave energy from irreversible energy conversion through an explicitly prescribed dissipative mechanism.

Collectively, the results establish a set of complementary energy-transfer diagnostics and conservation constraints relevant to the analysis of Alfvénic dynamics. However, the individual calculations do not yet constitute a fully self-consistent model of RSAE evolution. Establishing the combined effects of intermode coupling, energetic-particle feedback, thermal-species response, and dissipation on RSAE stability requires integrated kinetic simulations that evolve the wave fields and particle distributions consistently.

The derived diagnostics provide a foundation for future investigations of RSAE saturation and energetic-particle transport, as well as for the development of physics-informed state-estimation and inverse-design approaches for fusion-plasma operating conditions.

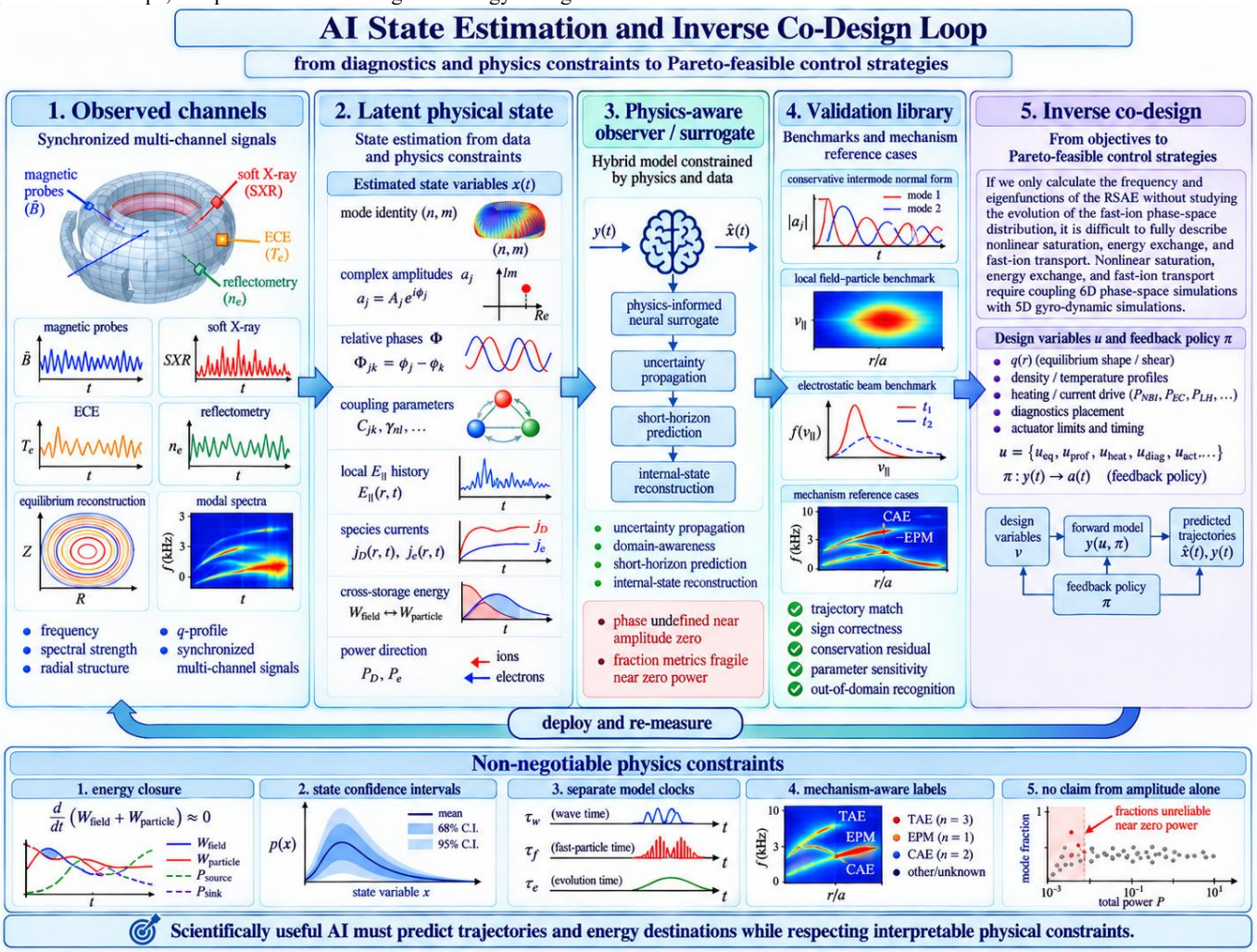


Figure 38 | Conceptual framework for physics-informed stateestimation and inverse co-design. Conceptual workflow for physics-informed inverse co-design framework of fusion-plasma operating conditions. Multichannel diagnostics are used to infer latent physical states, including modal amplitudes and phases, coupling parameters, and species-resolved energy-transfer directions. Physics-constrained surrogate models are validated against reduced numerical benchmarks before being incorporated into an inverse-design and feedback-control framework. Energy conservation, uncertainty quantification, and mechanism-specific validation provide the principal physical constraints.

References

[1] Chen, L. & Zonca, F. Physics of Alfvén waves and energetic particles in burning plasmas. *Reviews of Modern Physics* **88**, 015008 (2016). https://doi.org/10.1103/RevModPhys.88.015008

[2] Zonca, F., Chen, L., Briguglio, S., Fogaccia, G., Vlad, G. & Wang, X. Nonlinear dynamics of phase space zonal structures and energetic particle physics in fusion plasmas. *New Journal of Physics* **17**, 013052 (2015). https://doi.org/10.1088/1367-2630/17/1/013052

[3] Van Zeeland, M. A. et al. Reversed shear Alfvén eigenmode stabilization by localized electron cyclotron heating. *Plasma Physics and Controlled Fusion* **50**, 035009 (2008). https://doi.org/10.1088/0741-3335/50/3/035009

[4] Van Zeeland, M. A. et al. Measurements, modelling and electron cyclotron heating modification of Alfvén eigenmode activity in DIII-D. *Nuclear Fusion* **49**, 065003 (2009). https://doi.org/10.1088/0029-5515/49/6/065003

[5] Wei, S., Wang, T., Chen, N. & Qiu, Z. Nonlinear reversed shear Alfvén eigenmode saturation due to spontaneous zonal current generation. *Journal of Plasma Physics* **87**, 905870505 (2021). https://doi.org/10.1017/S0022377821000908

[6] Ma, R. et al. How zonal fields suppress reversed shear Alfvén eigenmode in tokamak plasmas. *Physical Review Letters* **137**, 045101 (2026). https://doi.org/10.1103/hh65-rgwv

[7] Liu, P. et al. Cross-scale interaction between microturbulence and meso-scale reversed shear Alfvén eigenmodes in DIII-D plasmas. *Nuclear Fusion* **64**, 076007 (2024). https://doi.org/10.1088/1741-4326/ad4809

[8] Breizman, B. N., Berk, H. L., Pekker, M. S., Pinches, S. D. & Sharapov, S. E. Theory of Alfvén eigenmodes in shear reversed plasmas. *Physics of Plasmas* **10**, 3649–3660 (2003). https://doi.org/10.1063/1.1597495

[9] Edlund, E. M. et al. Observation of Reversed Shear Alfvén Eigenmodes between Sawtooth Crashes in the Alcator C-Mod Tokamak. *Physical Review Letters* **102**, 165003 (2009). https://doi.org/10.1103/PhysRevLett.102.165003

[10] Sharapov, S. E. et al. MHD spectroscopy through detecting toroidal Alfvén eigenmodes and Alfvén wave cascades. *Physics Letters A* **289**, 127–134 (2001). https://doi.org/10.1016/S0375-9601(01)00588-6

[11] Gorelenkov, N. N., Kramer, G. J. & Nazikian, R. Combined ideal and kinetic effects on reversed shear Alfvén eigenmodes. *Physics of Plasmas* **18**, 102503 (2011). https://doi.org/10.1063/1.3640691

[12] Shi, Y., Qin, H. & Fisch, N. J. Three-wave scattering in magnetized plasmas: From cold fluid to quantized Lagrangian. *Physical Review E* **96**, 023204 (2017). https://doi.org/10.1103/PhysRevE.96.023204

[13] Shi, Y. Three-wave interactions in magnetized warm-fluid plasmas: General theory with evaluable coupling coefficient. *Physical Review E* **99**, 063212 (2019). https://doi.org/10.1103/PhysRevE.99.063212

[14] Manley, J. M. & Rowe, H. E. Some general properties of nonlinear elements—Part I. General energy relations. *Proceedings of the IRE* **44**, 904–913 (1956). https://doi.org/10.1109/JRPROC.1956.275145

[15] Brizard, A. J. & Hahm, T. S. Foundations of nonlinear gyrokinetic theory. *Reviews of Modern Physics* **79**, 421–468 (2007). https://doi.org/10.1103/RevModPhys.79.421

[16] Brizard, A. J. Exact conservation laws for gauge-free electromagnetic gyrokinetic equations. *Journal of Plasma Physics* **87**, 905870307 (2021). https://doi.org/10.1017/S0022377821000519

[17] Frieman, E. A. & Chen, L. Nonlinear gyrokinetic equations for low-frequency electromagnetic waves in general plasma equilibria. *The Physics of Fluids* **25**, 502–508 (1982). https://doi.org/10.1063/1.863762

[18] Hu, W. et al. Active real-time control of Alfvén eigenmodes by neutral beam and electron cyclotron heating in the DIII-D tokamak. *Nuclear Fusion* **58**, 124001 (2018). https://doi.org/10.1088/1741-4326/aaddaf

[19] Rothstein, A. et al. Initial testing of Alfvén eigenmode feedback control with machine-learning observers on DIII-D. *Nuclear Fusion* **64**, 096020 (2024). https://doi.org/10.1088/1741-4326/ad64e6

[20] Harris, C. R. et al. Array programming with NumPy. *Nature* **585**, 357–362 (2020). https://doi.org/10.1038/s41586-020-2649-2

[21] Hunter, J. D. Matplotlib: A 2D Graphics Environment. *Computing in Science & Engineering* **9**, 90–95 (2007). https://doi.org/10.1109/MCSE.2007.55

Methods

Computational programs and numerical conventions

Each figure group was generated by internally developed Python-based numerical codes in COIOS_PlasmaFusion_Pilot, implementing equilibrium reconstruction and ideal-MHD calculations, conservative wave coupling, local gyroaveraged thermal-species response, guiding-centre characteristics and electrostatic Vlasov–Poisson models. NumPy [20] supplied quadrature, Fourier transforms and complex linear algebra; Matplotlib [21] plotted saved arrays. Real quantities and complex amplitudes used float64 and complex128. Initial conditions, boundaries and normalization were specified for each model, with provenance records linking each figure to its source code, input parameters, and numerical output.

Throughout, reduced time is $\tau = \Omega_{\mathrm{ref}} t$: the three-wave model uses $\Omega_{\mathrm{ref}} = \kappa_0$ (reference nonlinear coupling rate), the local thermal model uses $\Omega_{\mathrm{ref}} = k_{\parallel} v_{\mathrm{th},e}$ (electron parallel transit rate), the beam model uses $\Omega_{\mathrm{ref}} = \omega_p$ (reference plasma angular frequency), and the pendulum resonance uses $\Omega_{\mathrm{ref}} = \sqrt{\alpha U}$ (small-amplitude bounce angular frequency). This convention specifies time steps and observation windows relative to each process's characteristic scale; $\omega_p t$ in the original figures is equivalent to τ for that example. Three-wave energies are normalized by the initial carrier total E_0. Thermal species use $v_{\mathrm{th},a} = \sqrt{2T_a/m_a}$, with free energy and power in the reference volume reported in J and W. Beam length and velocity units are $v_{\mathrm{ref}}/\omega_p$ and v_{ref}. Global MHD, guiding-centre and continuum figures use physical time.

Equilibrium and global ideal responses

For Figure 2, we solved fixed-boundary Grad–Shafranov equilibrium in an ellipse of major radius 3 m and horizontal/vertical semiaxes 1/1.2 m, with $\psi = 0$ at the boundary, a smooth axis and 2π toroidal periodicity. Defining $u = -\psi$, $u_a = \max u$, $s = 1 - u/u_a$ and $F = RB_\varphi$, the pressure input was $p = p_a(1-s)^2$ with $p_a = 2000\,\mathrm{Pa}$, and the current function was the positive root specified by $F^2 = F_b^2 + 2C_J u_a[g_0(1-s) + h(1/6 - s^2/2 + s^3/3)]$, with $F_b = 9\,\mathrm{T\,m}$, $C_J = 2.3\,\mathrm{T}$ and $(g_0, h) = (0.2,6)$; the broad-current control used $(g_0, h) = (1.0,0.2)$. The code used $FF' = -C_J[g_0 + hs(1-s)]$ and $p' = -2p_a(1-s)/u_a$, a degree-24 Chebyshev–Galerkin basis with a zero-boundary factor, and 36×224 squared-radius–angle quadrature. With $x = (R - 3\,\mathrm{m})/(1\,\mathrm{m})$, $y = Z/(1.2\,\mathrm{m})$ and initial guess $u = 0.3(1 - x^2 - y^2)$ Wb, Picard relaxation 0.3 reached relative coefficient change 10^{-11} in 73 iterations; q used 321×256 surface–angle integration. Independent 58×257 quadrature gave relative force-balance/GS residuals $1.64 \times 10^{-5}/1.08 \times 10^{-7}$, and degree $22 \to 24$ changed q curvature by 4.43×10^{-7}.

Figure 3 used this equilibrium, $n_D = n_e = 10^{19}(1 - 0.5s)\,\mathrm{m}^{-3}$, $n = 2$ and adiabatic index $5/3$, with axis regularity and zero wall-normal displacement. Full-vector displacement was expanded in regular disk Jacobi–Ritz spaces, comparing $|m| \le 9$, $k \le 4,5,6$, with $|m| \le 11$ angular checks; Cholesky mass transformation preceded Hermitian diagonalization. Initial displacement vanished, and archived near-q-minimum and inner-control velocity vectors were each normalized to $10^{-6}\,\mathrm{J}$ and embedded by basis labels. Positive-frequency components propagated analytically to $80\,\mu\mathrm{s}$; energy was recorded every $0.05\,\mu\mathrm{s}$, and full-angle RMS velocity reconstructed every $0.5\,\mu\mathrm{s}$ on 321×256 surface–angle points. Ten trajectories gave maximum relative energy drift/equation residual $7.97 \times 10^{-10}/2.29 \times 10^{-9}$. The plotted quantity is an initial-value response in finite Ritz spaces, with spatial sensitivity characterized by the $k = 5,6$ difference.

The independent frozen-equilibrium driven calculation in Fig. 4 used the same ellipse, uniform deuterium density $10^{19}\,\mathrm{m}^{-3}$, $n = 2$ and zero wall displacement in every component. Cubic C^1 Hermite radial elements with regular centre patches were compared at 16, 24, 32 and 40 elements, with poloidal cutoff 12, 18 radial Gauss points per element and 160 angles. Zero initial displacement/velocity was driven by $\rho\omega_s^2 \boldsymbol{\xi}_s e^{-i\omega_s t}$ at $17.72\,\mathrm{kHz}$ with source-amplitude reference $10^{-4}\,\mathrm{J}$. Analytic forced convolution in the complete eigenbasis propagated through $225.7\,\mu\mathrm{s}$ at 4001 saved nodes; the plot shows real radial displacement for 40 elements at $\varphi = 0$. Independent trapezoidal external-work integration gave maximum defect $5.51 \times 10^{-10}\,\mathrm{J}$, or 5.35×10^{-8} of peak field energy; the source shape's mass-projected/direct energy ratio was 28.19.

Three-wave integration and receiving-mode-frequency scan

Figures 6–10 integrated the normal-form right-hand side with in-house classical fourth-order Runge–Kutta, using $g = 1$, $\delta = 0$, $a_1(0) = a_2(0) = 1$ and $d(0) = b_0 e^{-i\Phi_0}$. Initial-power comparisons used $b_0 = 0.05,0.15,0.25,0.5$; trajectories and phase scans used $b_0 = 0.25$, 65 phases on $[-\pi, \pi]$, $\Delta\tau = 0.01$ and $\tau \le 12$. Power came directly from the right-hand side, turning points from invariant equations, and event times from linear interpolation between nodes. Phases $\pi/2$, 0.37 at steps 0.02/0.01/0.005 gave error-reduction factors 16.17/16.46; forward/reverse analytic-orbit amplitude errors were 5.81×10^{-11} / 1.69×10^{-10}. Across 157 trajectories including four-mode and control cases, maximum relative drift in the carrier-energy invariant (verify the missing mathematical symbol) were $1.12 \times 10^{-9}/2.12 \times 10^{-9}$.

Figure 11 used the same integrator, window and step with initial state $(a_1, a_2, d_3, d_4) = (1,1,-0.2i,-0.2i)$, receiving-mode couplings $1/\sqrt{2}$ and detunings $\pm\Delta/2$; Δ sampled 0–4 in increments of 0.125, giving 33 points. At each time, projection onto $B = (d_3 + d_4)/\sqrt{2}$ and $D = (d_3 - d_4)/\sqrt{2}$ supplied $2|D|^2/E_0$, with zero orthogonal energy at zero splitting as a control.

Common-field thermal-species calculations

The local collisionless deuterium–electron slab in Figs. 12–20 used outboard-midplane parameters at $s = 0.3815$: $B = 2.444\,\mathrm{T}$, $n_D = n_e = 8.093 \times 10^{18}\,\mathrm{m}^{-3}$, $T_D = T_e = 295.1\,\mathrm{eV}$ and $k_{\parallel} = 0.08818\,\mathrm{m}^{-1}$, with reference volume $1\,\mathrm{m}^3$. One conjugate Fourier pair had parallel period $2\pi/k_{\parallel}$; zero-flow Maxwellians used $h_D = 10^{-6} G_D$, $h_e = 0$, initial $A_{\parallel} = 0$ and quasineutral ϕ. Composite Simpson quadrature on each species' $[-6,6]v_{\mathrm{th}}$ interval used 65/513 deuterium/electron nodes, with 24-point deuterium perpendicular Gauss–Laguerre quadrature and 64 gyro-ring angles. Field sampling, charge/current moments and polarization shared quadrature weights; a 2×2 field Schur system advanced distributions and both potentials simultaneously by implicit midpoint. The scan $k_\perp \rho_D = 0.5,0.6,\ldots,1.5$ used $\Delta\tau = 0.04,0.02$ through 40, yielding 2000 fine-step power midpoints per scale; the independent main example in Fig. 20 used 1000 stored temporal sampling points.

Quadrature checks increased electron velocity nodes to 1025, extended their domain to $[-7,7]v_{\mathrm{th,e}}$, increased the deuterium grid to 129×32 and gyroangles to 128. Main-case relative total-free-energy drift was 4.85×10^{-14}; halving the step gave relative RMS changes in ϕ / $A_{\parallel}$ of 2.16×10^{-4} / 5.95×10^{-4} and changed cumulative particle-to-field return by 4.23×10^{-4}; velocity-node and domain refinements changed potential by less than 8.1×10^{-14}. Discrete deuterium/electron memory kernels in Fig. 12 differed from analytic expressions by at most $3.33 \times 10^{-15}/3.22 \times 10^{-15}$; in Fig. 13, discrete/analytic Γ_0 differed by at most 1.51×10^{-14}.

Thermal-species statistics evaluated electron, deuteron ion and combined electromagnetic-field powers at common midpoints; positive and negative powers were summed separately with time-step weights, preserving gross exchange and net change. Conditional release fractions used all $P_e < 0$ midpoints as denominator, and full-window occurrence fractions used all midpoints. Figure 15 normalized each scale by its peak electron-release power and used logarithmic bins with equal midpoint weights; colour gives bin counts divided by all electron-release midpoints. Figure 16 uses two times from one fine-step trajectory, and Fig. 17 normalizes each case by its initial free energy.

Self-consistent electrostatic electron beam

Figures 21–22 and 31–33 evolved two electron populations on the periodic spatial interval $0 \le x < 2\pi/0.3$ and velocity interval $-9 \le v \le 9$, with zero velocity-face flux and a fixed positive background. Bulk/beam density fractions, drift speeds and Gaussian standard deviations were $0.9/0.1$, $0/4.5$ and $1/0.5$, respectively; discrete velocity normalization preceded multiplication by $1 + 0.01\cos(0.3x)$. The grid was 65×256, the step 0.01 and final time $\tau = 100$; Figs. 31–33 use the same trajectory at $\tau = 0{,}50{,}100$, displaying $1 \le v \le 7$.

The in-house cell-average finite-volume program used monotonized-central MUSCL upwind fluxes and third-order strong-stability-preserving Runge–Kutta, recomputing the zero-mean Poisson field from charge density by FFT at every stage. Spatial/velocity/temporal refinements changed the first field peak by 0.2871% / 0.0110% / 0.000142% ; baseline maximum energy/particle-number drifts were $0.1926\%/2.95 \times 10^{-13}$. Linear growth/Maxwellian damping differed from independent dispersion roots by $0.656\%/0.937\%$, establishing quantitative accuracy for early excitation and the first peak; late filaments are reported as distribution evolution on the stated grid.

Axisymmetric forced spatial response

Figures 23–26 used cycle-averaged momentum stress from a frozen $17.72\,\mathrm{kHz}$ wave with prescribed pump-mode energy $10^{-4}\,\mathrm{J}$ as a constant force on an axisymmetric ideal response with zero initial displacement/velocity and zero displacement at the fixed elliptical wall. The discretization used 32 continuous cubic radial elements with analytic regular centre functions, real Fourier cutoff $m = 8$, and 14 radial Gauss/ 96 angular quadrature points per element. Cholesky reduction and Hermitian diagonalization retained 4848 directions for analytic propagation; strain rate, magnetic field and pressure were reconstructed on 40×128 flux–angle points. Of the 201 saved times, the state at $112.8\,\mu\mathrm{s}$ is displayed. Maximum relative work–energy residual was 6.00×10^{-15}; cutoff $6 \to 8$ changed velocity/strain rate/work by 15.44% / 28.58% / 1.58%, quantifying spatial representation sensitivity.

Guiding-centre orbits and particle-weighted orbit-field coupling spectrum

Figures 27–28 integrated nonrelativistic deuterium guiding-centre characteristics in a static reversed-shear equilibrium. Four-dimensional Halton quadrature sampled the invariant distribution below with temperature $80\,\mathrm{keV}$, reference density $10^{15}\,\mathrm{m^{-3}}$, momentum modulation 0.8 and elliptical radius 0.65–0.93; parallel-momentum/magnetic-moment domains used $200\,\mathrm{keV}$ reference cutoffs and included the guiding-centre Jacobian. Toroidal angles were periodic; particles reaching $s \ge 0.995$ at step endpoints exited with escaped energy recorded separately. RK4 used step $100\,\mathrm{ns}$ through $60\,\mu\mathrm{s}$, with $50\,\mathrm{ns}$ invariant checks. Figure 27 representative trajectories selected from the zero-probe orbit ensemble, classified by full-window net poloidal winding and parallel-momentum reversals.

The distribution was $F_0(E, P_\varphi) = Ce^{-E/T_h}\{1 + \alpha\tanh[(P_\varphi - P_c)/\Delta P]\}$, with $C = n_h[m_D/(2\pi T_h)]^{3/2}$, $\Delta P = 0.10e|\psi_{\mathrm{axis}}|$ and $P_\varphi = e\psi + p_\parallel R b_\varphi$. The reference P_c was evaluated on the sampled minimum-q surface at zero geometric poloidal angle and $v_\parallel = 0.7\sqrt{2(100\,\mathrm{keV})/m_D}$. The prescribed complex vector-potential profile was $\hat{A}_\parallel = A_{\mathrm{amp}} e^{-(s-s_c)^2/(2\sigma_s^2)}[(R - R_a - i(Z - Z_a))/L_0]^5 e^{2i\varphi}$, with $A_{\mathrm{amp}} = 2 \times 10^{-5}\,\mathrm{T\,m}$, $s_c = 0.7776$, $\sigma_s = 0.12$ and $L_0 = 1\,\mathrm{m}$; R_a, Z_a denote the magnetic axis. The interaction in Eq. (22) was $h_{1i} = -ev_{\parallel i}\hat{A}_\parallel(\mathbf{X}_i)$, set to zero after particle exit.

Figure 28 used 8192 zero-probe orbit calculations performed independently of the field-coupled evolution, combining eight initial toroidal phases through axisymmetry. Trapezoidal time–Fourier quadrature of the prescribed $n = 2$, geometric $m = 5$ probe interaction supplied the per-orbit coefficients in Eq. (22), whose squared magnitudes were summed with physical particle weights. Frequencies spanned $20 - 200\,\mathrm{kHz}$ at $2\,\mathrm{kHz}$ intervals; the $60\,\mu\mathrm{s}$ window gave resolution scale $16.67\,\mathrm{kHz}$. Nested $2048/4096/8192$ orbits peaked at $88/86/78\,\mathrm{kHz}$, with maximum adjacent shift $8\,\mathrm{kHz}$; the finest sample had effective peak count 117.1 and top-ten contribution 21.14%, quantifying sampling concentration in the occupied spectrum.

Trajectories and distributions in a prescribed resonance

Figures 29–30 advanced Hamilton's equations associated with Eq. (23) using an in-house implicit variational midpoint scheme, with fixed-point tolerance 10^{-12} and at most 32 iterations. Six orbits began at zero phase with actions $0.35{,}0.9{,}1.5{,}1.9{,}2.3{,}-2.5$, using step 0.02 for 1000 steps to $\tau = 20$. Figure 30 evaluated initial density along backward characteristics on 320×401 phase–action nodes, with periodic phase and action interval $I \in [-4{,}4]$, at $\tau = 0{,}4{,}8$. The initial state below was normalized with 128-point Gauss–Legendre quadrature; its energy bound $|I| \le 2.691$ keeps trajectories within the display window.

With $z = (I - 0.7)/1.1$, the initial action envelope was $b(z) = \exp[-1/(1 - z^2)]$ for $|z| < 1$ and zero elsewhere. The density was $f_0(\theta, I) = [1 + 0.25\cos\theta]b(z)/(2\pi N)$, where $N = 1.1\int_{-1}^{1} b\,(z)\,\mathrm{d}z$. Its support was therefore $I \in [-0.4{,}1.8]$, its phase period 2π and its total probability 1.

Steps $0.04/0.02/0.01$ gave an orbit-endpoint difference ratio 4.000 and maximum single-orbit energy error 1.42×10^{-4}. The density integral at $\tau = 8$ was 1.000 at the displayed precision; sampling $160 \times 201 \to 320 \times 401$ changed it by 7.25×10^{-4}, and steps $0.04/0.02$ gave density L^1 difference 5.41×10^{-4}, quantifying density sampling and orbit integration, respectively.

Continuum evolution and viscous reception

Figures 34–35 used the independent-surface limit, covering $0.55 < s < 0.94$ in the frozen equilibrium with 768-point Gauss–Legendre quadrature; 128 angles and tangential Fourier basis $|m| \le 16$ formed a 66-dimensional eigenproblem per surface. The initial $n = 2$, geometric $m = -5$ shear perturbation, centred at the q minimum with Gaussian width 0.055, was projected at initialization onto modes of frequency $\le 100\,\mathrm{kHz}$ and perpendicular mass fraction > 0.7, then normalized to $1\,\mathrm{J}$. Cholesky–Hermitian eigenmodes propagated by analytic complex phases to $0.8\,\mathrm{ms}$; 3201 outputs supplied 100 selected states, with endpoints shown. Surface refinement $384 \to 768$ changed coherent-energy histories by at most $1.67 \times 10^{-4}\,\mathrm{J}$; on 192 surfaces, poloidal cutoff $12 \to 16$ changed them by at most $1.87 \times 10^{-6}\,\mathrm{J}$.

Figures 36–37 retained one occupied shear branch per surface from the same low-frequency input, using radial differences of the complete three-component basis to form a positive-semidefinite edge operator. Runs used 768 surfaces, 128 angles, natural zero radial viscous traction and prescribed scalar kinematic viscosities $0{,}0.002{,}0.01{,}0.05\,\mathrm{m^2/s}$. Implicit midpoint advanced displacement/velocity, an in-house $LDL^\dagger$ factorization solved the Hermitian tridiagonal step matrix, and heat was accumulated independently from nonnegative dissipative work on grid edges at every step. Adjustment of the final integration step to align with theprescribed endpoint. Figure 37 used $\nu = 0.01\,\mathrm{m^2/s}$ at 100 saved states to plot cumulative heat per unit flux label, $\mathrm{d}Q_\nu/\mathrm{d}s$. Prescribed viscosity defines a passive thermal receiving-mode in this model.

Table 2 compares spatial and temporal refinement differences in final heat; the existing 17 calculations gave maximum wave-plus-heat residual $3.253 \times 10^{-13}\,\mathrm{J}$.

Kinematic viscosity ν $(\mathrm{m^2/s})$	Heat change for surfaces $384 \to 768$ (%)	Heat change for step $100 \to 50\,\mathrm{ns}$ (%)
0.002	1.272	0.00662
0.01	0.130	0.00299
0.05	0.00718	0.00130

Code and reproducibility record

The accompanying provenance record links each figure to its computational module, configuration, arrays, figure source and historical verification. The pendulum-resonance batch recorded Python 3.11.15 and NumPy 2.2.6; other batches are identified by their saved configurations and outputs. Historical and current continuum sources are retained under distinct hashes, with historical figures anchored to original arrays and run metadata.